Geophysical Journal International

Geophys. J. Int. (2024) **237,** 679–696
Advance Access publication 2024 February 15
GJI Heat Flow and Volcanology

https://doi.org/10.1093/gji/ggae054

Subsurface anatomy of the Irazú–Turrialba volcanic complex, inferred from the integration of local and ambient seismic tomographic methods

E. A. Jiwani-Brown [1], I. Koulakov [2], F. Muñoz-Burbano,[1] J. F. Pacheco,[3] M. M. Mora [4], G. Savard[1] and M. Lupi [1]

[1] *Department of Earth Sciences, University of Geneva,* 1204*, Geneva, Switzerland. E-mail: elliot.jiwani-brown@unige.ch*
[2] *Trofimuk Institute of Petroleum Geology and Geophysics SB RAS, Prospekt Koptyuga* 3, 630090*, Novosibirsk, Russia*
[3] *Observatorio Vulcanológico y Sismológico de Costa Rica (OVSICORI), Universidad Nacional Costa Rica, Heredia, Costa Rica*
[4] *Red Sismológica Nacional (RSN), Escuela Centroamericana de Geología, Universidad de Costa Rica, San José, Costa Rica*

Accepted 2024 February 14. Received 2024 January 30; in original form 2024 May 31

SUMMARY

Irazú and Turrialba are a twin volcanic complex that marks a distinct stop in volcanism along the Central America volcanic arc. We present a new traveltime velocity model of the crust beneath Irazú and Turrialba volcanoes, Costa Rica, and interpret it considering the results of previous ambient noise tomographic inversions. Data were acquired by a temporary seismic network during a period of low activity of the Irazú–Turrialba volcanic complex in 2018–2019. Beneath the Irazú volcano, we observe low *P*-wave velocities ($V_P = 5$ km s^{-1}) and low velocity ratios ($V_P/V_S = 1.6$). In contrast, below the Turrialba volcano, we observe low *S*-wave velocities ($V_S = 3$ km s^{-1}) and a high V_P/V_S ($= 1.85$) anomaly. We found that locations of low V_P and V_S anomalies (-15 %) correspond well with shear wave velocity anomalies retrieved from ambient noise tomography. At shallower depths, we observe high V_P and V_S anomalies ($+15$ %) located between the summits of the volcanoes. Subvertical velocity anomalies are also observed at greater depths, with high V_P and V_S anomalies appearing at the lower limits of our models. We propose a complex structure of an intermediate magmatic reservoir, presenting multiphase fluid states of a liquid-to-gas transition beneath Irazú and a juvenile store of magmatic fluid beneath Turrialba, while shallow fluid transport provides evidence of magmatic–hydrothermal interactions.

Key words: Earthquake ground motions; Seismic tomography; Volcanic arc processes; Magma chamber processes; Physics of magma and magma bodies.

1 INTRODUCTION

Modern seismology provides a multitude of methods to investigate volcanic settings. The deployment of ground motion studies, either from seismic (Husen *et al.* 2003; Arroyo *et al.* 2009; Dinc *et al.* 2010) or from geodetic (Marshall *et al.* 2000; Carvajal-Soto *et al.* 2020) means, has helped the understanding of quasi-real-time activity levels within volcanic environments. Costa Rica is probably one of the most instrumented and monitored country in Central America, highlighting the importance of permanent, up-to-date and well-maintained monitoring networks.

Passive seismic tomographic studies are relatively affordable, low-maintenance and non-intrusive experiments. They provide images of the velocity structure of the subsurface across multiple scales. Due to the complex tectonics, and risk from seismic and volcanic hazards, Costa Rica has been subject to a number of different multidisciplinary studies. Geodetic studies observe complex surface deformation in central Costa Rica (Freymueller *et al.* 1993; Kellogg *et al.* 1995; Lundgren & Russo 1996; LaFemina *et al.* 2009; Kobayashi *et al.* 2014) (Fig. 1a). Ground motion measurements indicate a tectonic escape in the form of a forearc sliver, and the emergence of a microplate, away from the indented, buoyant, reheated Cocos Ridge (Carvajal-Soto *et al.* 2020). Gazel *et al.* (2019) propose a transition from oceanic to the juvenile continental crust at the junction between the Cocos–Caribbean subduction margin and the Panama microplate (Fig. 1a). Several seismic experiments provide insights into the crustal structure of central Costa Rica using receiver functions (Yao *et al.* 1999; Dzierma *et al.* 2010; Villegas Alvarez *et al.* 2019). Other passive seismic studies shed light on the central Costa Rican Pacific subduction margin (Husen *et al.* 2003; Arroyo *et al.* 2009; Dinc *et al.* 2010). The Irazú–Turrialba volcanic complex (ITVC) forms the largest stratovolcano edifice in central Costa Rica (Reagan *et al.* 2006; Carr *et al.* 2007; DeVitre *et al.* 2019). The ITVC marks a gap in the volcanism of Central America

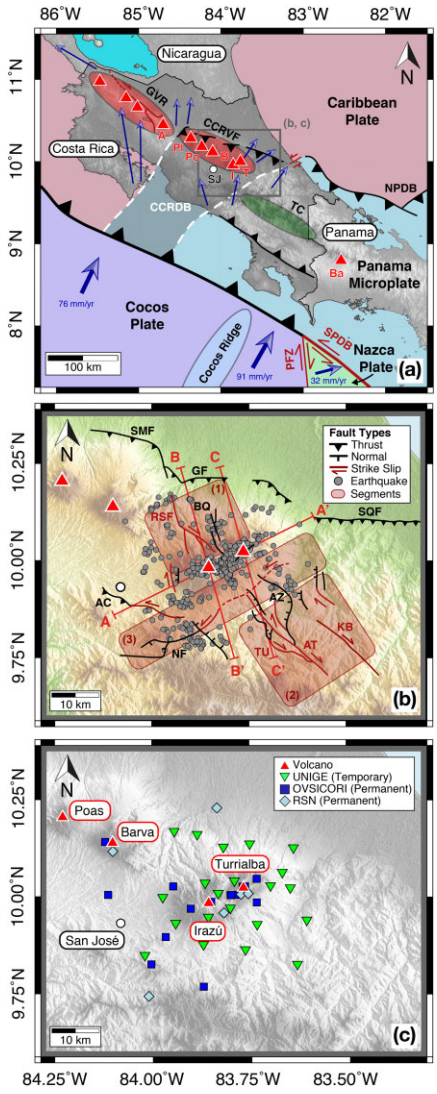

Figure 1. Central Costa Rica study region with key tectonic features and major plate motions. (a) Regional-scale tectonic setting of Costa Rica and (b) local-scale tectonic setting of ITVC, complete with pre-inversion event/source locations, greyed dots, recorded by the seismic network. Axes of the cross-sections (A–A′, B–B′ and C–C′) that appear throughout the study are also plotted. (c) Distribution of the seismic stations deployed during the study period. The networks of OVSICORI, RSN and UNIGE are shown by squares (blue), diamonds (azul) and triangles (green). The key tectonics are shown: North Panama Deformation Boundary (NPDB), South Panama Deformation Boundary (SPDB) and Pacific Fracture Zone (PFZ). The blue arrows represent plate motions relative to the Caribbean plate (modified after Carvajal-Soto *et al.* 2020). The large, white dashed line on the regional map represents the potential region of the Central Costa Rica Deformation Belt (CCRDB). The volcanic edifices (red triangles and ellipses) include the Guanacaste Volcanic Range (GVR) and CCRVF, while the continental mountain range of the Talamanca Cordillera is shown by the green ellipses. The marked volcanoes are Arenal (A), Platanar (Pl), Poás (Po), Barva (B), Irazú (I) and Turrialba (T). The capital city of San José is also indicated. Montero *et al.* (2013b) separate the ITVC fault system into three principal segments: (1) the Río Sucio segment, including the Río Sucio (RSF) and Blanquito (BQ) faults to the northwest; (2) the Atirro–Tucurrique segment, including the Atirro (AT), Tucurrique (TU), Azul (AZ) and Kabebeta (KB) faults to the southeast; and (3) a central pull-apart basin accommodated within the ITVC and along the Navarro (NF) and Aguacaliente (AC) faults. Main features adapted from Alvarado *et al.* (2017), Montero *et al.* (2013b) and Denyer (2009).

(Protti *et al.* 1996; MacMillan *et al.* 2004) and the termination of the central Costa Rica volcanic front (CCRVF; e.g. LaFemina *et al.* 2009; Gazel *et al.* 2019; Jiwani-Brown *et al.* 2022). Geodetic studies have primarily focused on the large-scale tectonic plate motions and crustal deformation, highlighting the diverse seismic behaviours along the Cocos and Caribbean subduction margin (LaFemina *et al.* 2009; Kobayashi *et al.* 2014; Carvajal-Soto *et al.* 2020).

Local earthquake tomography (LET) imaging is a common tool to investigate volcanic environments and is a relatively high-resolution method that has helped to effectively map the subsurface velocity structure of multiple magmatic systems (e.g. Koulakov 2009; Koulakov *et al.* 2013; Kasatkina *et al.* 2014; Bushenkova *et al.* 2019; García *et al.* 2019). LET uses seismic waves released by local earthquakes that are iteratively inverted to produce a model of the V_P and V_S wave seismic velocity distributions as well as the V_P/V_S ratio. Such velocity models can provide information linked to the composition, compressibility or physical state (e.g. lithology, rheology, fluid content, principal stress and strain) of the subsurface, as well as indicate any presence of fluids (i.e. magma, gas or groundwater). LET studies in Costa Rica have previously focused on subduction (Husen *et al.* 2003; Dinc *et al.* 2010) and seismogenic (e.g. fault; DeShon *et al.* 2006) structures. However, due to the lack of a dedicated seismic network, LET has rarely been applied to investigate Costa Rican volcanoes. Rabbel *et al.* (2011) determined that notable anisotropic variations occurred across the transition from oceanic to continental morphology and subducting slab, affecting the ability to resolve large-scale features.

Ambient noise tomography (ANT) studies (Nuñez *et al.* 2020; Jiwani-Brown *et al.* 2022) have been implemented in Costa Rica, suggesting a number of shared reservoir systems at intermediate crustal depths (Lücke *et al.* 2010; DeVitre *et al.* 2019; Jiwani-Brown *et al.* 2022). While Nuñez *et al.* (2020) performed a regional-scale ANT, Jiwani-Brown *et al.* (2022) produced a local-scale ANT of the ITVC. Jiwani-Brown *et al.* (2022) propose that at about 6 km depth, a low-velocity zone may be representative of a common magmatic reservoir for the Irazú and Turrialba volcanoes. This reservoir is suggested to be surrounded by a ductile zone. From here, magmas may migrate upwards into shallower small-scale reservoirs (possibly below the detection limits of Jiwani-Brown *et al.* 2022) feeding Irazú and Turrialba volcanoes. These two reservoirs would account for the variation in magma composition observed by Benjamin *et al.* (2007), Di Piazza *et al.* (2015) and de Moor *et al.* (2016).

LET and ANT are both passive seismic methods, used to map subsurface velocity structures. Surface waves retrieved from ambient noise are most suited to resolve large, lateral variations in the crustal V_S structure, whereas *P* and *S* waves released by local earthquakes are sensitive to sharp velocity discontinuities at depth. In practice, within some limits, the two methods can reveal similar large-scale structures like magmatic reservoirs that create notable discontinuities laterally and vertically. Given their different yet complementary sensitivities, integrating the two methods could provide a more robust interpretation of subsurface features, particularly in heterogeneous settings such as volcanic environments (Shirzad & Shomali 2015; Zhang *et al.* 2020; Chen *et al.* 2021). Previous studies where both methods have been performed separately have been done at Avacha, Russia (Koulakov *et al.* 2014; Bushenkova *et al.* 2019), Katla, Iceland (Jeddi *et al.* 2016, 2017), Toba, Indonesia (Stankiewicz *et al.* 2010; Jaxybulatov *et al.* 2014; Koulakov *et al.* 2016) and Klyuchevskoy, Russia (Koulakov *et al.* 2011; Green *et al.* 2020; Koulakov *et al.* 2020b; Egorushkin *et al.* 2021) volcanoes. They have been used to study complex topography (Hartzell *et al.* 2014), basin environments (Lehujeur *et al.* 2021), industrial seismic

hazard assessments (Parolai *et al.* 2001) and also volcanic systems (Shomali & Shirzad 2015). Recent studies (Parolai *et al.* 2001; Shomali & Shirzad 2015; Lehujeur *et al.* 2021) revealed high levels of agreement between ANT and LET.

This study produces V_P, V_S and V_P/V_S models of the ITVC and surrounding regions using LET. We compare them with the ANT results of Jiwani-Brown *et al.* (2022). We assess the reliability of both methods while gauging whether these two inversion tools can be complimentary to each other and provide mutually consistent results within the same volcanic environment and using the same seismic network. Finally, we propose an integrated conceptual model of the plumbing system of the ITVC.

2 GEOLOGICAL CONTEXT AND METHODOLOGY

2.1 Seismo-tectonic setting

The Central America volcanic arc is a succession of volcanoes extending from Guatemala to Panama. This volcanism is due to the oblique subduction of the Cocos plate beneath the Caribbean plate (DeMets 2001; Kobayashi *et al.* 2014; Álvarez-Gómez *et al.* 2019; Carvajal-Soto *et al.* 2020). The convergence of the Cocos and Caribbean plates promotes a number of geological processes (Molnar & Sykes 1969; Stoiber & Carr 1973; Sallarès *et al.* 2000; Norabuena *et al.* 2004; Dzierma *et al.* 2010, 2011; Fig. 1a). Geodetic studies showcase the complex ongoing deformation. Correa-Mora *et al.* (2009), LaFemina *et al.* (2009), Franco *et al.* (2012), Kobayashi *et al.* (2014), Staller *et al.* (2016) and Carvajal-Soto *et al.* (2020) determined the existence of the Central America forearc bloc. This tectonic sliver propagates parallel to the volcanic arc and perpendicular to the axis of subduction, to the northwest. DeMets *et al.* (2010) noted that the formation of the Panama microplate was also a consequence of the combination of oblique subduction and the divergence of the Nazca plate (Freymueller *et al.* 1993; Kellogg *et al.* 1995; Lundgren & Russo 1996; Carvajal-Soto *et al.* 2020). Convergence of the Panama microplate and the Caribbean plate is defined by the North Panama deformed belt (NPDB; Silver *et al.* 1990; Camacho *et al.* 2010). The accommodation of deformation due to this complex plate interaction is believed to occur within the disputed region of deformation known as the Central Costa Rica Deformation Belt (CCRDB; Carvajal-Soto *et al.* 2020). Such a deformation belt results in notable zones of strike-slip seismicity at shallow depths (<20 km) (Marshall *et al.* 2000; Montero 2001; Montero *et al.* 2013b; Alvarado *et al.* 2017; Jiwani-Brown 2023) defining a zone of complex, diffuse active faulting.

The Cocos subducting slab is morphologically diverse and varies in dip angle along the axis of subduction (Alvarado *et al.* 2017). To the northwest, the Cocos oceanic crust is steeper dipping and smoother topographically. To the southeast, the crust is rougher due to a succession of seamounts and the Cocos ridge subducting directly below central and southern Costa Rica (Carr *et al.* 2003; Alvarado *et al.* 2007; Hoernle *et al.* 2008; Gazel *et al.* 2009). The complex slab morphology becomes more buoyant after subduction due to a combination of the younger oceanic Cocos plate, reheating of the Cocos ridge, and collision with the Panama microplate (LaFemina *et al.* 2009). Gazel *et al.* (2019) notes an important transition at the coincidence of the subducted Cocos ridge and ITVC and the subsequent onset of the Talamanca cordillera to the southwest. The Talamanca cordillera consists of uplifted juvenile continental crust (Gazel *et al.* 2009, 2019, 2021).

The ITVC lies within 70 km of densely populated regions, the current capital city of San Jose (Fig. 1b) and the previous capital, Cartago, further to the southeast. Despite the proximity to the volcanic cones, eruptive cycles differ between Irazú and Turrialba volcanoes (Di Piazza *et al.* 2015). Irazú is now in a period of relative quiescence (Epiard *et al.* 2017) and is suggested to undergo eruptive cycles of about 200–400 yr (Alvarado *et al.* 2006). Turrialba is active and features a well-developed summit and hydrothermal system. Eruptive products have been characterized as basaltic and andesitic (Vaselli *et al.* 2010; Campion *et al.* 2012; Mick *et al.* 2021). After remaining quiescent for more than a century, reactivation occurred in 1996, until a first phreatomagmatic explosion occurred in January 2010 (Martini *et al.* 2010; Vaselli *et al.* 2010; Campion *et al.* 2012; van der Laat *et al.* 2022). Vaselli *et al.* (2010) and Martini *et al.* (2010) defined three phases of activity between 1996 and 2010, consisting of a seismic-fumarolic stage, followed by increased seismicity and ground deformation, and finally increased fumarolic output, dominated by magmatic fluids. Magmatic-hydrothermal interaction was also confirmed by Vaselli *et al.* (2010) and Martini *et al.* (2010) who found that the hydrothermal system had removed magmatic components from seismically induced fumarolic activity during the second phase of pre-eruptive activity between 2001 and 2007. Since then, the activity has evolved from phreatic to magmatic, in a series of distinct eruptive phases reflecting the path towards the open-vent phase in 2016 (van der Laat *et al.* 2022).

The CCRVF, and in particular the ITVC, have evidence of geochemically enriched magmas due to the subduction of the Cocos ridge and offshore Galapagos traps (Hoernle *et al.* 2008; Gazel *et al.* 2009, 2021). This consists of mostly recycled intraplate materials and basalts rich in trace elements (Gazel *et al.* 2021). Di Piazza *et al.* (2019) study of petrological data determined that magma in the ITVC consisted of andesitic products stored in a main reservoir at ∼13 km depth, often perturbed by injections of deeper basaltic magma (Alvarado *et al.* 2006). Further geochemical and petrophysical studies explore the previous volatility and future potential for eruptivity of both Irazú and Turrialba volcanoes (Alvarado *et al.* 2006; Benjamin *et al.* 2007; Gazel *et al.* 2009; DeVitre *et al.* 2019; Di Piazza *et al.* 2019). Results indicate a diversity of volcanism, promoting variability in eruptivity and complex regions of magma storage beneath the subsurface. This includes zones of increased ductile behaviour and the interconnection of unknown structures within a crystalline mush, with mobile lenses of intrusive bodies, including sills and dikes (Cashman *et al.* 2017; Ebmeier *et al.* 2018; Edmonds *et al.* 2019). Cooler wedge temperatures suggest that these regions of melt are spatially spread over large areas beneath the volcanic front (Rychert *et al.* 2008; Syracuse *et al.* 2008; Abers *et al.* 2014).

2.2 Seismic network

We deployed 20 broad-band seismic stations in a network surrounding the ITVC (Fig. 1c). The sensors consisted of three-component Nanometrics Trillium Compact (20 s and 120 s) seismometers. The experiment ran from April 2018 to March 2019. All stations were equipped with Omnirecs DATA-CUBE3 digitizers, recording continuous ground motion at a sampling rate of 100 Hz. The temporary network integrated two regional permanent networks, namely 16 stations from the Observatorio Vulcanológico y Sismológico de Costa Rica (OVSICORI) of the Universidad Nacional Autonoma de Costa Rica and 6 from the Red Sismológica Nacional (RSN) of the Universidad de Costa Rica (RSN 2011) (Fig. 1c).

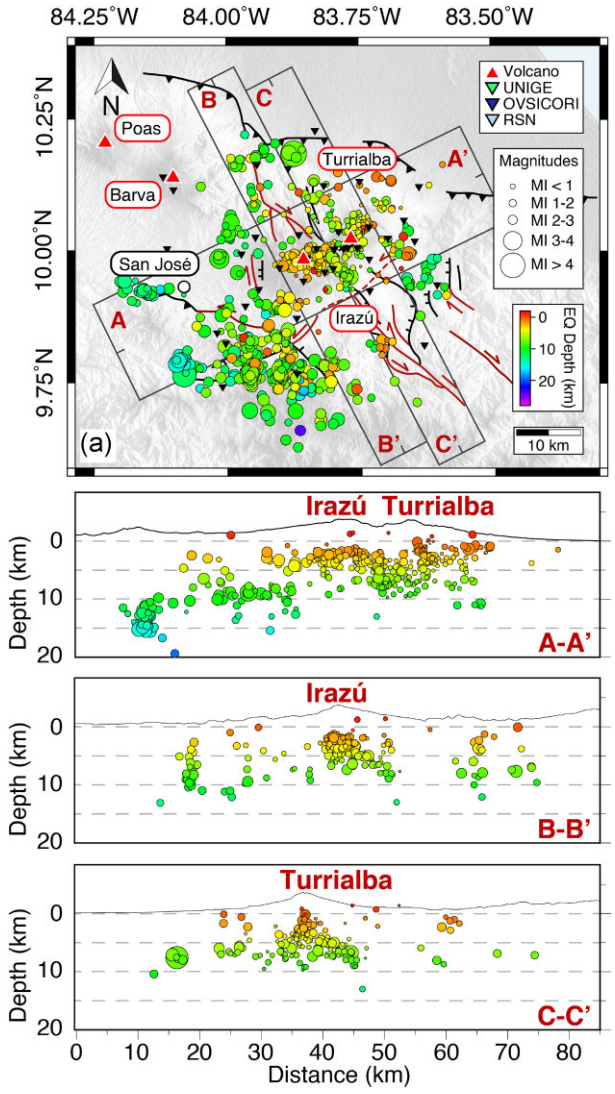

Figure 2. Location of seismic events from the dedicated network. Relocated seismicity taken from data recorded on our temporary and permanent stations during the study period, adapted from Jiwani-Brown (2023). The lower panels show cross-sections along the axis of the ITVC (A–A′) and perpendicularly for Irazú (B–B′) and Turrialba volcanoes (C–C′).

Fig. 2 presents seismicity recorded within our network over the 11-month period. Jiwani-Brown (2023) present a detailed interpretation of the seismicity, relocation of events and focal mechanisms of this catalogue. Only events falling within a 50 km radius from the centre of our network are chosen for this LET study. We also constrain the catalogue to satisfy certain selection criteria, also explained in more detail by Jiwani-Brown (2023). Our final data set consists of 24,681 phase readings (12,738 *P*- and 11,943 *S*-wave arrival times) from 1050 local events.

2.3 LET algorithm

For the LET, we use the tomographic algorithm LOTOS (Local Tomography Software), designed for simultaneous inversions of V_P and V_S velocity structures and source coordinates (Koulakov 2009). We perform iterative inversions using LOTOS for V_P and V_S velocity values and arrival time parameters, and source locations based on the arrival times of body waves from local earthquakes. The inversion also derives the V_P/V_S ratio from the independent V_P and V_S velocities. Damping parameters (smoothing and amplitude regularization) are determined from synthetic tests with checkerboard models and realistic noise distributions. The checkerboard tests are also used to assess the resolution of the inverted velocity structure. We use synthetic modelling to optimize the damping and misfit parameters, and reinforce the reliability of the recovered real-data models.

We use as a starting 1-D structure derived by Jiwani-Brown (2023) from a *P*-wave traveltime inversion of local earthquakes using the software *Velest*, a Fortran routine designed to derive 1-D velocity models for earthquake location (Kissling *et al.* 1994, 1995). We also tested regional-scale velocity models from Quintero & Kissling (2001) and Sallarès *et al.* (2000). However, after repeated tests, we used the local 1-D model as it is closer to the local velocity structure, therefore aiding the convergence of the inversion. We selected our data for the inversion based on a minimum of 5 phases recorded per event and a maximal difference of 1.7 s between absolute *P* and *S* phase times. Using these parameters reduced our number of events to 904 local events, and 12,161 *P*- and 11,346 *S*-wave arrival time phases.

Similarly to Koulakov *et al.* (2013), Kasatkina *et al.* (2014) and Bushenkova *et al.* (2019), we calculate 5 iterations of the LOTOS code. Increasing the number of iterations has a similar effect as decreasing the damping value. This number of iterations is chosen as a compromise between computational cost and minimization of non-linear effects. We also improve the resulting 3-D tomography variance reduction. Each iteration within the LOTOS workflow (joint earthquake re-location and inversion of velocity) uses a least-squares (LSQR) algorithm (Paige & Saunders 1982) and the updated 3-D velocity model from the previous iteration to determine the final 3-D velocity model presented in the results. Source relocation and calculations of the new velocity structure is carried out using an algorithm that solves for bending ray traces (Um & Thurber 1987). Inversions performed for V_P and V_S velocities are made using the algorithm derived by Koulakov *et al.* (2007). From the derived seismic velocities we calculated the V_P/V_S ratio.

The LOTOS code uses an adaptive mesh parametrization with nodes spacing and distribution proportional to the ray density (Koulakov *et al.* 2013). The minimal grid spacing is predefined at 3 km laterally and at 1.5 km at depth. We performed the mesh calculations at 4 different geographic bearings (0°, 22°, 45° and 67°), merged into a single model. Calculating at these bearings avoids artefacts pertaining to grid orientations (Thurber *et al.* 2009; Koulakov 2009).

3 VERIFICATION OF THE MODEL

We used various tests to assess the spatial resolution and the chosen free parameters of the model. Free parameters are experimentally or theoretically estimated variables of a mathematical model and include the smoothing and misfit parameters needed to constrain the most accurate model when compared to the real data. This parametrization allows us to determine if the obtained solutions are suitable for the given initial model, and parameters used in the calculations. The optimal resolution given the configuration of stations is important as it determines the minimum size of seismic velocity anomalies that can be interpreted.

3.1 Odd/even test

We performed an odd/even test (e.g. Koulakov *et al.* 2010, 2013; Kasatkina *et al.* 2014) to determine the stability of the final velocity model. This involves splitting the data set into two groups of equal size and obtaining two independent inversions using the same parameters as for the complete data set. The data set is arbitrarily split using the event ID, namely even ID numbers for one group and odd ID numbers for the other. The odd/even test is meant to assess noise levels in the observed data. If the odd and even inversion results produce inconsistent velocity anomalies, this indicates that random noise could be contaminating the data. The results of the odd/even test are presented in Fig. 3 as reconstructions of the V_P/V_S ratio. We see that for all the main observable anomalies (later described in more detail in Section 4) there is no difference between the odd and even subsets.

3.2 Checkerboard test

To determine the effective resolution of our network, and provide the limits to any potential observable small-scale structures from the results, we performed a series of checkerboard tests (Rawlinson *et al.* 2014). These are synthetic models with alternating high and low velocities (e.g. Koulakov *et al.* (2013); Rawlinson & Spakman (2016)). The workflow and damping parameters used for the inversion of the synthetic traveltime data are the same as for the observed data. Using the same ray path distribution as for the observed data, we calculate the traveltimes through the checkerboard model using a 3-D ray bending algorithm. The checkerboard model consists of the superposition of the 1-D reference model and 3-D anomalies of 5 km by 5 km in size and ± 7 % amplitude. These synthetic traveltimes are then perturbed by noise relating to remnant residuals after the final inversion to reproduce the level of noise in the observed data. Changing the size of the high/low anomalies in the checkerboard model allows us to determine the minimum size of the anomaly we can observe. Horizontal map view slices and vertical depth sections of the recovered checkerboard models (Figs 4 and 5) reveal that within the central part of the study area, the 5 km anomalies are resolved well, particularly at shallow depths. As the depth increases, vertical smearing of the velocity pattern is notable, and offsets in the relocated sources occur as a consequence of trade-offs between data and model variance reduction. We achieve resolution of 5 km vertical anomalies up to depths of 10 km, while resolution increases to 10 km lateral anomalies between 6 and 10 km depth. There is a loss of resolution at the edges of our inversion grid, corresponding also with the boundary of our seismic network.

3.3 Realistic structures test

Our final verification test is to simulate anomalies of realistic configuration for magma chambers beneath the ITVC (Figs 5g and h). We present the V_P/V_S ratio test as it is the most significant for our interpretation. We defined anomalies as a set of polygons in the vertical A–A′ cross-section. These synthetic anomalies represent a simplified interpretation of the plumbing system based on results from the experimental data inversion. We applied an addition of 10 % random noise to account for local traveltime variations at each station. We resolved the most significant structures. However, we could not resolve features smaller than 5 km, such as the conduit connecting the shallow and intermediate depth high V_P/V_S ratio anomalies beneath Turrialba. The resolution of main structures supports the reliability of these realistic synthetic tests and generally concurs with the realistic data inversion discussed below. The results of the three synthetic modelling methods (odds/evens, checkerboard, realistic structures) improve the confidence in the data set and the verification of resolvable features.

4 RESULTS OF THE TOMOGRAPHIC INVERSION

The residuals between computed and real data can be analysed by the variance reduction, which represents the quality of the data. Our variance reduction was 48 % and 52% for the V_P and V_S velocity data respectively. These reduction values are relatively high compared to previous small-scale tomographies on volcanoes (Kuznetsov & Koulakov 2014; García *et al.* 2019). Koulakov *et al.* (2013) also relates higher variance reductions to more numerous higher magnitude earthquakes, which can be picked with a higher accuracy. Our results are presented as horizontal depth slices (at 2, 4, 6 and 8 km depths, Figure 6) and vertical cross sections (Figure 7). We identify 7 significant velocity anomalies (Fig. 7), interpreted in more detail throughout the discussion. Anomaly 1 (A1, Figs 7a and d) is a low V_P (−15 %) and low low V_P/V_S ratio (1.6) (Fig. 7c) zone 30 km along both A–A′ and B–B′ at around 8 km depth below Irazú. Anomaly 2 (A2, Figs 7b and h) is a low V_S (−15%) and low low V_P/V_S ratio (1.85) (Fig. 7c) zone 40 km along A–A′ and 25 km along C–C′ at around 8 km depth below Turrialba. Anomaly 1 and 2 correspond with the most prominent absolute low velocity (V_P = 5.0 km s^{-1} and V_S = 3.0 km s^{-1} respectively) features (Fig. 8). The lateral extent of Anomaly 1 and Anomaly 2 overlap between the two volcanoes, with a relatively low V_P and V_S anomalies (−5 %). We discern a sharp transition in V_P/V_S ratio, from high (1.8) to low (1.6) separating the two anomalies at 35 km along profile A–A′. We also notice a higher concentration of earthquakes at the upper limit of these low V_S velocity anomalies and high V_P/V_S ratios.

Anomaly 3 is a low V_S (−15%) and high V_P/V_S ratio anomaly. It is at the summit of Irazú volcano, located 28 km and 30 km along profiles A–A′ and B–B′ respectively and at +2 km asl (A3, Figs 7b and e). Anomaly 4 is a high V_P (+15 %) and low V_P/V_S ratio anomaly. It is located between the active volcanic centres of Irazú and Turrialba, extending southwest from +3 km asl to 2 km depth, beneath Irazú and above Anomaly 1, 30 km along profiles A–A′ and C–C′ respectively and at +2 km asl (A4, Figs 7a, d and e). Noticeable high absolute velocities (V_P = 6.4 km s^{-1} and V_S = 3.6 km s^{-1}) are at the same location as Anomaly 4 (Fig. 8). Anomaly 5 is located on the eastern flank of Turrialba volcano, 40 km and 25 km along profile A–A′ and C–C′ respectively (A5, Figs 7a, b, g and h) and is characterized by high V_P and V_S (+20 %) anomalies. On the western flank of Turrialba volcano is the low V_P and V_S (−20 %) Anomaly 6, at 3 km asl, 35 km and 28 km along profile A–A′ and C–C′ respectively (A6, Figs 7a, b, g and h). The special distribution of Anomaly 2 and 6 suggests they could be linked.

Anomalies 3 and 6 coincide with Cluster 1 and 2 of relocated seismicity (C1 and C2 respectively, Figs 7c, f and i), spatially distributed above the intermediate depth Anomalies 1 and 2. Cluster 2 is also located beneath Anomaly 5, below the Turrialba summit at 2 km depth. A third sub-vertical cluster is observed equidistant from the two volcanoes at 4 km depth (C3, Figs 7c and i). From the depth slice (Figs 6 i–l), we see Anomaly 7, a low V_S and high V_P/V_S ratios north and east of the Turrialba volcanic summit, up to 8 km depth (A7, Figs 7a, b, g and h). However, these occur at the spatial limits of our study (Figs 4 and 5) and should be verified by further investigations.

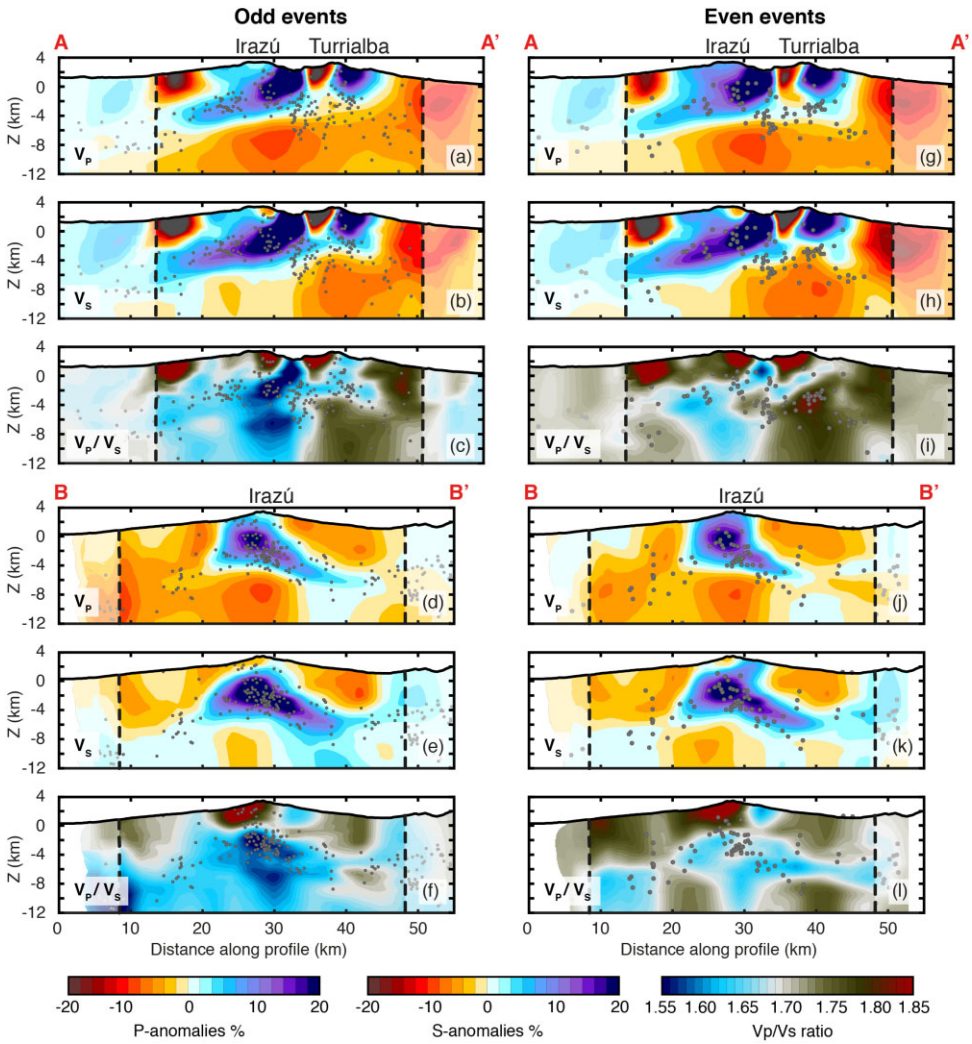

Figure 3. Odd/Evens synthetic test. Inversion results for two independent subsets of odd and even event numbers. Data are presented as cross-sections passing through the ITVC and Irazú, for V_P and V_S (e–h) velocity anomalies, and V_P/V_S ratio distributions.

5 DISCUSSION

5.1 Passive seismic tomographic imaging

Passive seismic tomography capitalizes on energy generated within the earth to provide a seismic velocity structure pertaining to particular geological domains. We can indirectly infer geological structures, fluids and fracturations that may occur within the medium. Although LET and ANT may have a shared target of investigation, discrepancies will naturally arise due to the different physical sensitivities of the wave types, and parametrization and regularization differences that exist within various inversion methodologies. LET implements information derived from body waves generated by earthquakes. For this, we measure the amplitude and location of both V_P and V_S velocity anomalies, and the relationship between the two in the form of V_P/V_S ratio. We use the V_P, V_S and V_P/V_S velocity structure to interpret subsurface features beneath the ITVC. Previous studies (e.g. Nicholson & Simpson 1985; Lees & Wu 2000; Lees 2007; Lesage *et al.* 2018) have shown that V_P provides mainly information about the medium's composition, while V_S and V_P/V_S ratio provide an indication of the compressibility factor, indicating, for example, the presence of fluids or fracture zones. We present a review of the main effects of V_P and V_S velocity distributions according to a number of previous investigations in Table 1. These parameters can also be used to interpret the level of activity and whether there is evidence of recent magmatic feeding in the volcanic system (e.g. Koulakov *et al.* 2013, 2014; Bushenkova *et al.* 2019; García *et al.* 2019). The LET relies on ray coverage associated with the propagation of seismic wave fronts, meaning lateral and depth resolution require a high number and a good distribution of seismic events within the aperture of the network (Li & Thurber 1995; Haslinger *et al.* 2001; Koulakov 2009; Thurber *et al.* 2009; Wu *et al.* 2009).

ANT makes use of surface waves generated by natural or anthropogenic sources (Brenguier *et al.* 2007; Harmon *et al.* 2008; Nicolson *et al.* 2012; Mordret *et al.* 2013). Because surface wave dispersion is primarily controlled by V_S structure, dispersion curves measured between multiple pairs of stations can be inverted for 3-D V_S models under some assumptions (e.g. constant Vp/Vs ratio and density). V_S anomalies derived from ANT are useful to indicate the presence of fluids and pressure–temperature conditions. Due to the depth-dependent sensitivity of surface waves and dispersion, shorter wavelengths are more sensitive to shallower structures, whereas at greater depths, the elastic properties of the medium are sampled by longer wavelengths (Xia *et al.* 2000). The control on spatial resolution for ANT is also dependent on

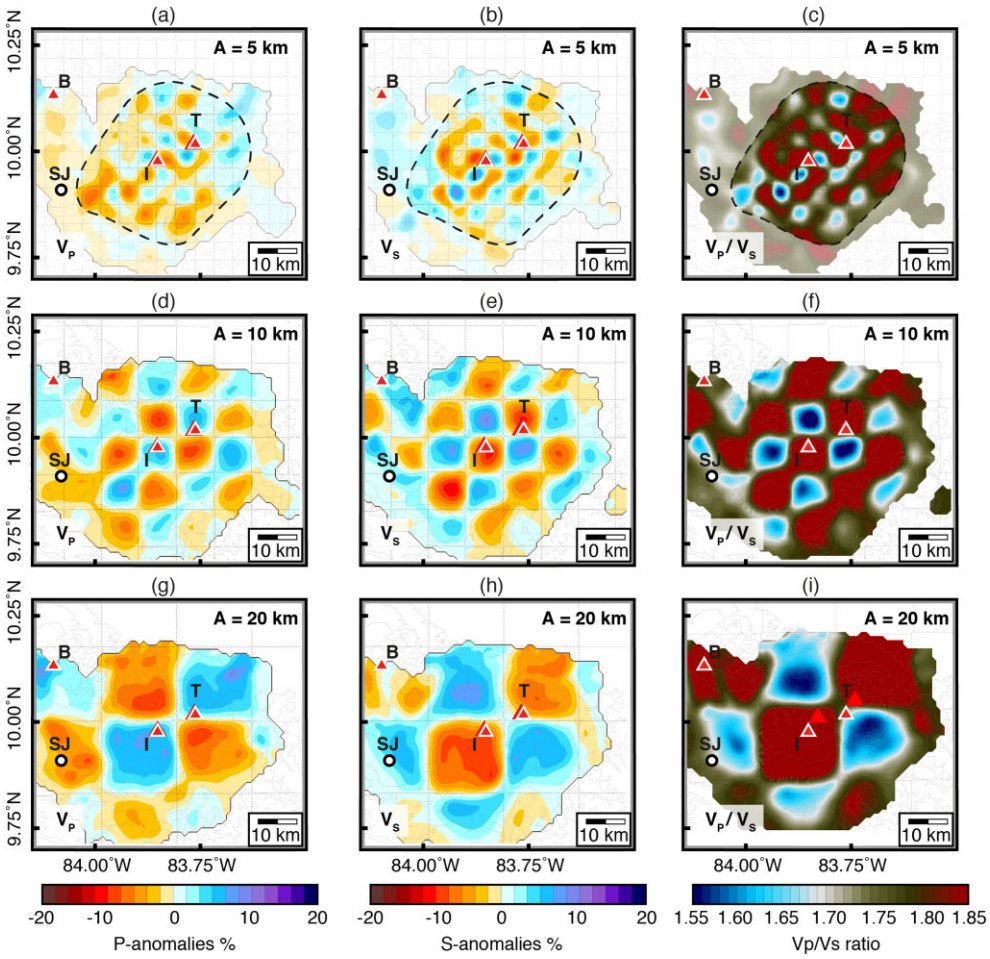

Figure 4. Horizontal resolution checkerboard synthetic test. Checkerboard resolution test at horizontal depth slice of $z = 4$ km, consisting of alternating 5 (a–c), 10 (d–f) and 20 (g–i) km wide squares of low and high velocity anomalies (±7 %). Dashed outline shows the resolvable area based on the smallest checkerboard size.

array geometry (and aperture), the frequency content of ambient noise measured by the sensors, and more importantly, the amplitude, distribution and directivity of noise (Shapiro *et al.* 2005; Lin *et al.* 2008; Brenguier *et al.* 2016; Lehujeur *et al.* 2016; Fallahi *et al.* 2017; Planès *et al.* 2020; Lehujeur *et al.* 2021; Calò *et al.* 2023).

Given that the source of energy of both techniques varies significantly across the two methods, it is important to understand the limits of both tomography methods. Zhang *et al.* (2020) and Lehujeur *et al.* (2021) compare both methods and determined that ANT will produce an improved vertical resolution with increasing depth. However, LET is better at resolving the outlines of magmatic bodies, and sharp fracture zones responsible for seismicity. If a spatial region is sampled by rays coming from a small range of directions, velocity anomalies will be smeared along this direction (Thurber *et al.* 2009; Koulakov 2009). As LET relies on earthquakes, inversion results can be more susceptible to smearing vertically if only shallow events are recorded. However, it can also provide a much more effective horizontal resolution. It is important to note, this is highly dependent on the distribution of earthquakes and therefore is study specific.

Multi-physics inversion approaches such as joint inversion of body and surface waves represent the next generation of passive seismic imaging (Sun *et al.* 2020). Because the sensitivity of body waves and surface waves are complimentary, joint inversion of these data sets into a common parametrization and regularization scheme would provide more robust and easier-to-interpret tomographic models. Several studies implementing joint inversion of body wave and surface wave data have shown that the resulting 3-D models are particularly improved for shallow subsurface structures and mitigate the trade-off between source parameters and velocity that can bias LET models (Zhang *et al.* 2014, 2020; Gao *et al.* 2022). The improvements of a more computationally complex and expensive joint inversion schemes over separate inversions are however sometimes modest and may in some cases not provide new information on the major structures of interest (Zhang *et al.* 2014). Future work could explore joint inversion of the body wave and surface wave data acquired at the Irazú and Turrialba volcanoes and assess potential improvements over the results presented in this study. Here, we prefer to compare the two models obtained from separate LET and ANT inversions and derive from them a unified interpretation while keeping in mind differences in resolution and inversion schemes.

5.2 Plumbing system of the ITVC inferred from LET data

We present several interpretations for the identified anomalies at 8 km depth, that could indicate the presence of a complex magmatic

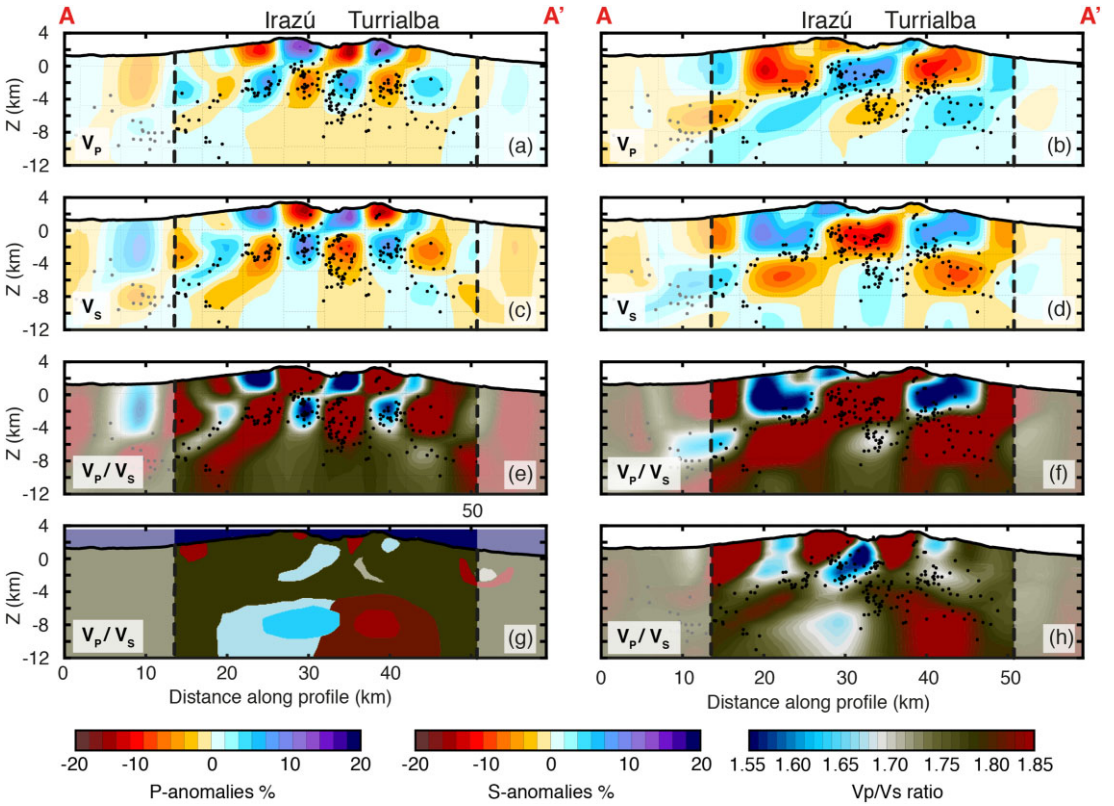

Figure 5. Vertical resolution synthetic tests. Checkerboard resolution test for vertical depth slices of the ITVC consisting of alternating 5 (a, c, e) and 10 (b, d, f) km wide squares of low and high velocity anomalies (±7 %). Dashed outline shows resolvable area based on the smallest checkerboard size. Original (g) and inversion (h) of synthetic test using realistic features.

reservoir beneath the Irazú and Turrialba volcanoes, with parts of the system differing in physical state (Figs 6 and 7). We suggest that the system is not a singular homogeneous reservoir, but consists of multiple magmatic bodies that are fed by a laterally varying source. This interpretation supports previous authors who propose a shared magmatic system occurs below the ITVC. Previous petrological (Di Piazza *et al.* 2019) and melt inclusion studies (Benjamin *et al.* 2007; Di Piazza *et al.* 2019) found eruptive products from both volcanoes presented properties that could be indicative of a shared reservoir. For example, Di Piazza *et al.* (2019) found andesitic magma from both systems formed at pressure and temperature conditions corresponding to a depth of ≈ 12 km below the eruptive centres, while Benjamin *et al.* (2007) and Di Piazza *et al.* (2019) estimate similar water contents within exhumed magma from both systems. Geodetic (Battaglia *et al.* 2019) and gravity (Lücke *et al.* 2010) data also suggest a shared magma reservoir.

We propose that the discrete transition of low to high V_P/V_S ratio characterized by Anomaly 1 and 2 (35 km along profile A–A′ at ≥ 4 km depth, Fig. 7c) indicates a multi-state magmatic system below the ITVC. The low V_S Anomaly 2 observed below the summit of Turrialba volcano may be indicative of higher fluid saturation levels (Nicholson & Simpson 1985; Lees & Wu 2000; Lees 2007; Lesage *et al.* 2018). The high V_P/V_S ratio suggests potential partial melt (Lees 2007; Koulakov *et al.* 2007; Kasatkina *et al.* 2014; Bushenkova *et al.* 2019) (Table 1). Similar V_S anomalies and high V_P/V_S ratio have been used to identify partial melts in various volcanic settings including Klyuchevskoy volcano (Koulakov *et al.* 2017), Nevado del Ruiz volcano (Vargas *et al.* 2017), Mount Spurr volcano (Koulakov *et al.* 2018) and in Kamchatka, Russia (Bushenkova *et al.* 2019). The V_P/V_S ratio and width of Anomaly 2 decreases with depth, indicating the sub-vertical elongation of a plumbing system culminating with the 8 km depth reservoir. The sub-vertical feature could also be explained by a decrease in vertical resolution. González-Vidal *et al.* (2018) suggest that similar plumbing systems of andesitic volcanoes may consist of superimposed dike complexes. Such a dike complex is compatible with our observations and the ones of previous authors (Cashman *et al.* 2017; Edmonds *et al.* 2019). Although these V_P and V_S anomalies are predominantly low, we observe a transition of relatively increasing V_P and decreasing V_S velocity anomalies as we move eastwards from Irazú to Turrialba (Figs 7a and b). Previous studies propose that low V_P anomalies in volcanic settings can also be attributed to hydrothermal alteration (Pola *et al.* 2012; Lesage *et al.* 2018). Similar values have also been attributed to critical transitions from liquid to gas due to decreasing pore pressure (Lees 2007; Lesage *et al.* 2018). This phase change is due to decompression (Christopher *et al.* 2015) and has been observed by decreasing V_P/V_S ratio values, for instance, in the LET results of Nevado de Huila volcanic complex in Colombia by García *et al.* (2019). We propose that Anomaly 1 beneath Irazú may represent an older, now cooling sub-horizontal sill-like melt intrusion, not currently fed by the deeper magmatic system. The lateral structure of these velocity anomalies may be explained by the extension of an intermediate magmatic reservoir beneath the Irazú and Turrialba volcanoes, in two distinct physical states of gas and liquid respectively. The immediate contrast from high to low V_P/V_S ratio could imply a distinct lack of liquid (or melt) transition occurring within this region, however the low V_P and V_S Anomaly 1 and 2 suggest a more gradual transition. These results correspond

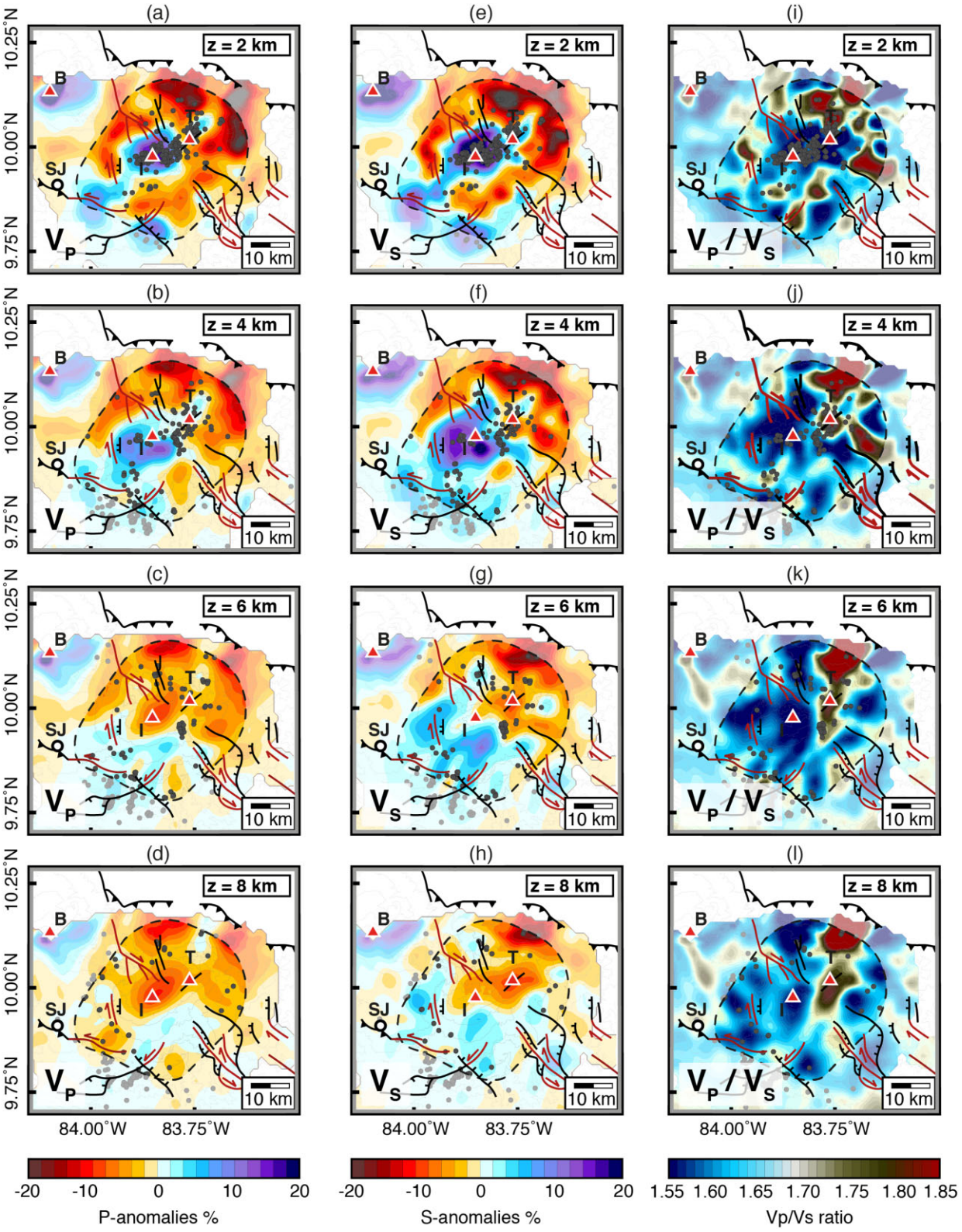

Figure 6. Horizontal velocity anomaly depth sections. Inversion results of the experimental data for V_P (a–d) and V_S (e–h) velocity anomalies, and V_P/V_S ratio distributions (i–l). The horizontal depth sections are at 2, 4, 6 and 8 km depth. The located sources for each depth interval are shown with dots, triangles represent the location of the active volcanic centres of Irazú and Turrialba. The main tectonic features from Fig. 1 are also indicated.

to DeVitre *et al.* (2019) who postulates a magmatic reservoir above 10 km depth, interpreted from gravity modelling (Lücke *et al.* 2010) and seismically induced degassing (Conde *et al.* 2014). Alvarado *et al.* (2006); Di Piazza *et al.* (2019) propose the existence of a mid-crustal, main feeding reservoir at ≈ 15 km depth. However, this is deeper than the vertical limits of our study.

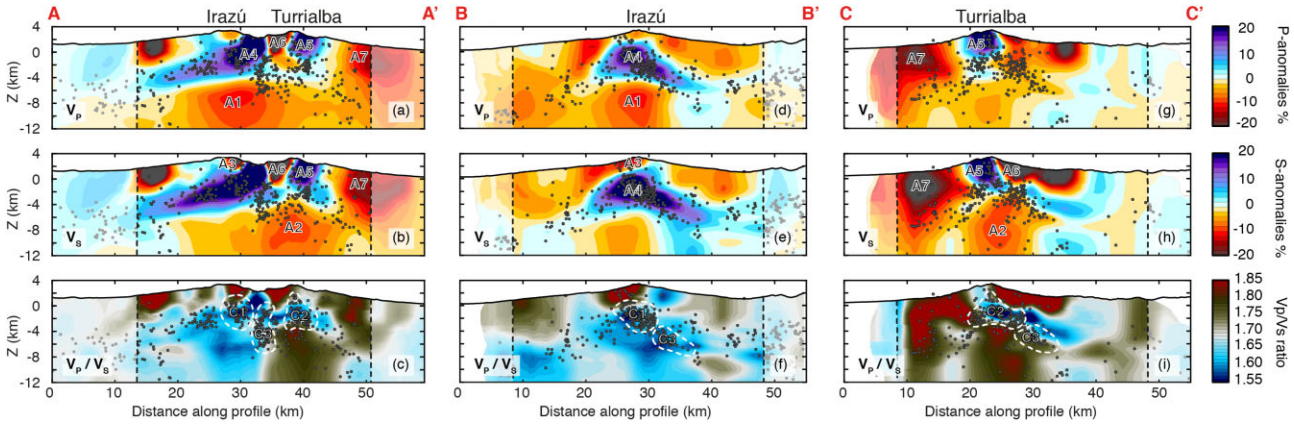

Figure 7. Vertical velocity anomaly cross-sections. Inversion results of the experimental data for V_P and V_S velocity anomalies, and V_P/V_S ratio distributions. Presented as vertical cross-sections parallel through and the ITVC (profile A–A′) (a–c), and perpendicular to the ITVC through Irazú (profile B–B′) (b–f) and Turrialba (profile C–C′) (g–i) up to a depth of 12 km. The located sources for each vertical section are shown with grey dots. Velocity anomalies (A) and seismic clusters (C) interpreted in the text are also plotted.

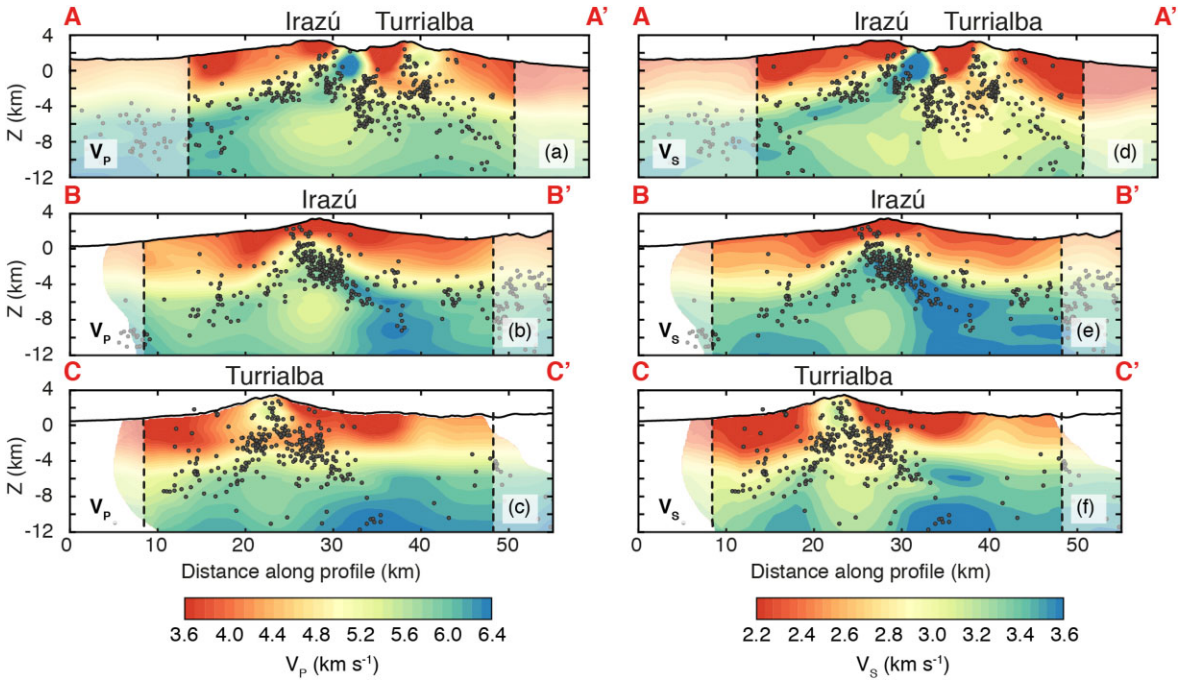

Figure 8. Vertical absolute velocity cross-sections. Inversion results of the experimental data for absolute V_P (a–c) and V_S (d–f) velocity values. Presented as vertical cross-sections parallel through and the ITVC (profile A–A′), and perpendicular to the ITVC through Irazú (profile B–B′) and Turrialba (profile C–C′) up to a depth of 12 km. The located sources for each vertical section are shown with grey dots.

The seismicity of Cluster 3 at 32 km along profile A–A′ and at 3 km depth (C1, Fig. 7c) of relocated seismicity also occurs between the high and low V_P/V_S ratios between Anomaly 1 and 2, indicating a region of brittle deformation at the shallow limits of this boundary. We propose that ductile deformation is promoted between these regions of low V_P and V_S, supported by a lack of seismicity. This provides physical evidence for a rheological separation from the surrounding host rock. We use the distribution of seismicity to infer the upwards migration of fluids through cracks and regions of brittle fracturation (van der Laat *et al.* 2022). Specifically, the spatial spread of the Cluster 2 seismicity is from the upper limit of Anomaly 2 at 4 km depth to the summit of Turrialba (Figs 7a–c and g–e). Cluster 2 (C2, Figs 7c and i) aligns with the acute transition between the high and low seismic velocity anomalies 5 and 6, respectively, 40 and 25 km along profile A–A′ and C–C′ (A5 and A6, Figs 7a, b, g and h). This sharp contrast and vertical alignment of seismicity could represent a fault or a domain accommodating the upward migration of fluids released from the intermediate depth, Anomaly 1 reservoir. Previous studies suggest that this may indicate the presence of gas (Takei 2002; De Siena *et al.* 2010; Lesage *et al.* 2018). In line with previous authors (Conde *et al.* 2014; de Moor *et al.* 2016; Kuznetsov *et al.* 2017; Koulakov *et al.* 2018; Bushenkova *et al.* 2019), we propose that such anomalies may be caused by the degassing magma and the active plumbing system of the ITVC. Branches of seismicity appear to settle beneath the lower depth (2 km) of Anomaly 6, suggesting the existence of a possible

Table 1. Review of major effects on V_P and V_S velocities, and V_P/V_S within a volcanic environment.

Cause	Effect on V_P	Effect on V_S	Further comments	Source
Temperature increase	Decrease	Decrease	V_P decreases less than V_S therefore V_P/V_S increases	(Lees 2007; Lesage *et al.* 2018)
Presence of fluid (e.g. mineral precipitation)	Decrease	Decrease	V_S decreases more than V_P therefore V_P/V_S increases	(Lees 2007; Adam & Otheim 2013)
Phase change (e.g. liquid to gas)	Decrease	Decrease	At phase transition critical temperature, significant V_P increase therefore decrease in V_P/V_S	(Takei 2002; Lees 2007; Adam & Otheim 2013)
Partial melt	Decrease	Decrease	V_P decreases less than V_S therefore V_P/V_S increases	(Iyer & Hirahara 1993; Lesage *et al.* 2018)
Hydrothermal alteration	Decrease	Uncorrelated	Caused by formation of new pores, clay minerals and change of interconnected cavities	(Pola *et al.* 2012)
Effective pore pressure increase (dry medium)	Increase	Increase	Closing of compliant microcracks	(Vinciguerra *et al.* 2005; Nara *et al.* 2011)
Effective pore pressure increase (saturated medium)	Decrease	Decrease	Opening of compliant microcracks due to reduction of effective pressure	(Vanorio *et al.* 2002)
Orientation with principal axis (perpendicular to σ_1)	Decrease	Decrease	V_P/V_S increases	(Heap *et al.* 2014)
Orientation with principal axis (parallel to σ_1)	Increase	Increase	V_P/V_S decreases	(Heap *et al.* 2014)
Compressibility increase (gas)	Increase	-	V_P/V_S decreases	(Lees 2007; Lesage *et al.* 2018)
Compressibility increase (liquid)	Decrease	-	V_P/V_S decreases	(Lees 2007; Lesage *et al.* 2018)
Igneous rock (felsic to mafic)	Increase	Increase	V_P decreases more than V_S therefore V_P/V_S increases	(Christensen 1996)

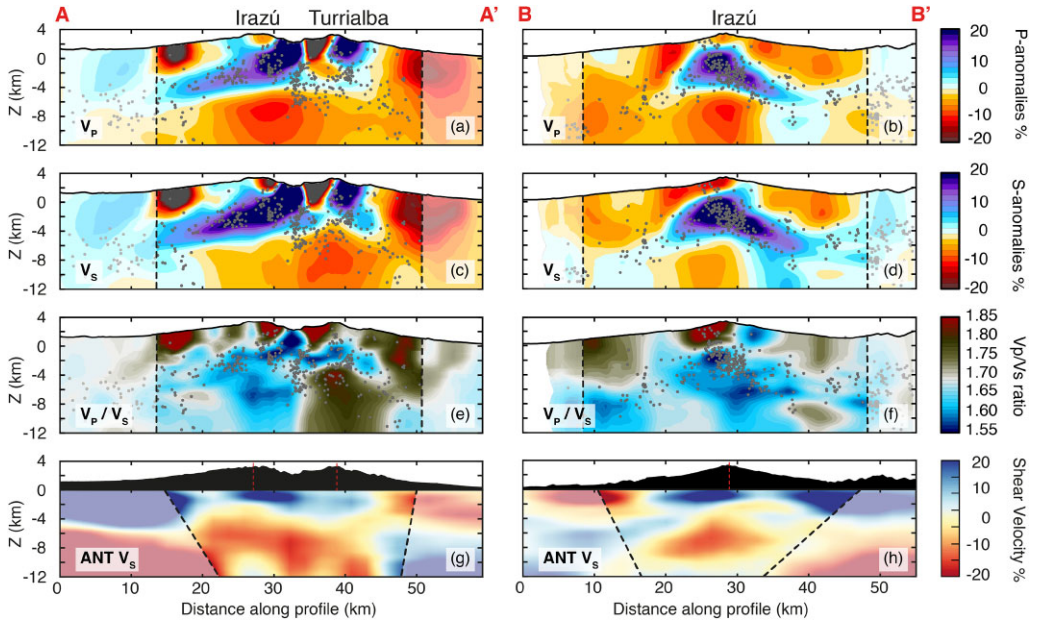

Figure 9. LET and ANT cross-section comparisons. Cross-sections of velocity anomaly models, presented as a comparison of results obtained from the LET (a–f) for the ITVC and Irazú with results from Jiwani-Brown *et al.* (2022) ANT (g–h) study. The black dashed lines delimit the area of preferred resolution for both studies.

shallow reservoir, 1 km beneath the summit of Turrialba. In this framework, the basaltic-andesitic magma storage region postulated by DeVitre *et al.* (2019) would accommodate the mixing between fresh and stagnant rhyolitic residual magma from previous eruptive events (de Moor *et al.* 2016; Rizzo *et al.* 2016).

We suggest that the shallow, high V_P velocity Anomaly 4 between the centre of the ITVC (2 km depth) may indicate the remnants of earlier episodic magmatism associated with the Irazú volcano. Montero *et al.* (2013b) remarked that volcanic activity during the late Quaternary interacted with the perpendicularly intersecting active strike-slip fault system (Río-Sucio, Azul and Tucurrique faults, Fig. 1b), and coincided with a significant increase in volcanic activity. The Finca Libres volcanic depression is a surface expression associated with eruptivity in the Quaternary at the ITVC (Montero *et al.* 2013a). In general, high-velocity structures in volcanic environments are explained by solidified or crystallized magmatic fluids (Berger *et al.* 2011; Shomali & Shirzad 2015). We suggest that Anomaly 4 could be evidence of the ancient, cooled magmatic intrusion responsible for the Finca Libres depression. High-velocity anomalies at shallow depths have previously been attributed to overpressured solidified igneous rock, for example in Popocatépetl volcano, Mexico (Kuznetsov & Koulakov 2014). Villegas Alvarez *et al.* (2019) used receiver functions to determine V_S structures beneath seismic stations deployed at Irazú volcano. They found notable high-velocity zones at similar depths ($\leq$ 5 km) to Anomaly 4, also attributing it to cooled portions of dense volcanic rocks. This high

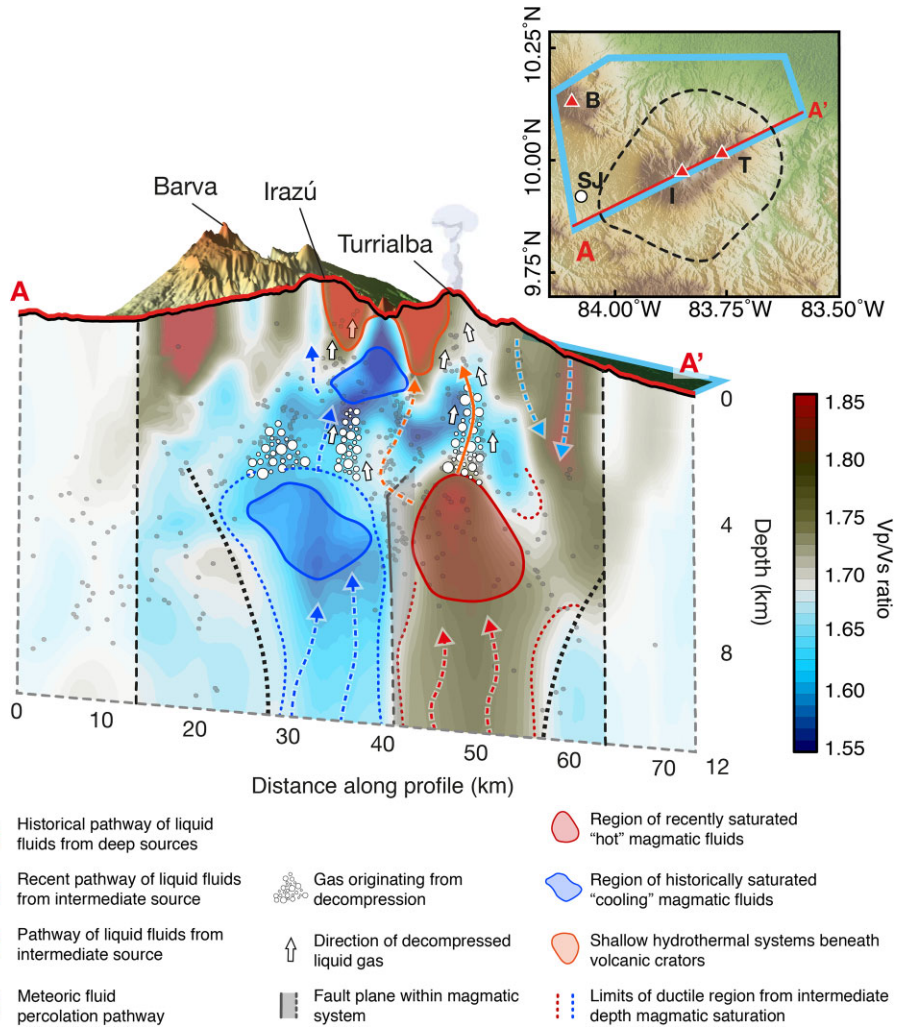

Figure 10. ITVC conceptual magmatic anatomy. Conceptual model of the feeding system beneath the ITVC. The interpretation made over the resultant 3-D V_P/V_S ratio distributions. Limits of low and high velocity anomalies, magmatic transfer zones and liquid fluid transfer zones are marked. Extent of ductile zone is shown with black dotted lines. Grey dots show the localized seismic events. Vertical scale is exaggerated to clearly highlight the subsurface features.

V_P and V_S anomaly also propagates beneath Irazú, and could present as a natural cap above the intermediate depth shared reservoir. A difference in physical state also supports the presence of this anomaly. We propose the contrast between Anomaly 1 and 3 explains the lack of recent activity beneath Irazú volcano, acting as a stopper for magmatism beneath Irazú and promotes the accumulation of magmatic fluid beneath Turrialba volcano, within this multi-state magmatic reservoir. Relocated seismicity is also notable within this anomaly. Decreasing thermal stresses on volcanic rock can reduce the medium's strength (Heap & Violay 2021), allowing for such non-elastic, brittle deformation, evident in other andesitic volcanoes such as Volcán de Colima (Heap *et al.* 2018). The seismicity of Cluster 1 associated with the high V_P Anomaly 4 also appears sub-vertical inferring a potential plane that facilitates slip. Jiwani-Brown (2023) produce a study of the seismicity over the same period as our LET and resolved fault solutions indicating principal horizontal stresses supporting a strike-slip regime in this region. Previous applications of LET for fault zones (Koulakov *et al.* 2010) revealed that the emplacement of bodies within a shallow, fractured fault zone such as that off the southeastern flank of Irazú (Villegas Alvarez *et al.* 2019), can be revealed by similar high-velocity anomalies.

Christopher *et al.* (2015) remark that large differences in viscosity and density can be attributed to the separation of melt and magmatic fluids during periods of eruptive stability. If this occurs, pressure in the system increases while crystallization in magma causes a counteracting contraction. We suggest the presence of upwardly migrating exsolving magmatic fluids, supported by the shallow, high V_P/V_S ratio Anomaly 3 below Irazú summit. Epiard *et al.* (2017) observed fumaroles and hot springs at Irazú in 2015, and recent reports from local monitoring authorities (OVSICORI-UNA 2020) have observed deflation of volcanic surface and the emergence of a crater lake from 2010 up until at least 2018. Processes associated with a deflating body could also be responsible for these shallow low-velocity values. Christopher *et al.* (2015) also state that this process occurs at timescales of 10^3 to 10^4 years. It is possible that the exsolution of fluids in the late-Quaternary volcanic deposits mentioned previously could be responsible for this.

The northern extent of the ITVC consists of a dense jungle and a vast array of river systems. It also experiences the second highest rainfall levels in Costa Rica (Waylen *et al.* 1996). We suggest that high V_P/V_S ratios (e.g. Anomaly 7) on the northern and eastern flanks of both volcanoes (and at the lateral extreme of our model) could be caused by a combination of unconsolidated magmatic rock

and shallow concentrations of down-welling waters. Previous observations by Koulakov *et al.* (2020a) and Koulakov *et al.* (2021) produce similar velocity anomalies, and propose that meteoric water penetrating into the volcanic edifice is the cause. These fluids could also penetrate onto the footwall of recorded thrust faults, e.g. the Siquirres fault (Fig. 1b). The LET study by Geoffroy & Dorbath (2008) also attributed high V_P/V_S ratio anomalies the deep percolation of meteoric fluids to depths up to 6 km in an oblique, transtensional volcano-tectonic environment. Studies by Crawford *et al.* (2013), Coulon *et al.* (2017) and Wilks *et al.* (2017) notice that when a hydrothermal system is formed, increases in volcano-tectonic seismicity are observed in volcanic environments. We do not observe a high number of earthquakes in this region, suggesting that there may not be any interactions between the magmatic system and potential meteoric fluids. These anomalies are also at the limit of our resolved area, which can affect the magnitude of these anomalies. Jiwani-Brown (2023) also noted that stations to the northeast of the network experienced the largest arrival time delays of almost 10 ms. This delay could be a consequence of an extreme change in topography and slower seismic velocities in the backarc basin.

5.3 ANT versus LET and final conceptual model

We present a comparison of our results obtained by LET to those achieved by Jiwani-Brown *et al.* (2022) using ANT imaging techniques in Fig. 9. To provide consistency and continuity, we used the same initial velocity model in this LET study as that used for the ANT (Jiwani-Brown *et al.* 2022). However, as there is a trade-off between the average velocity models and the origin of the sources, the effects on the final model will be much greater on the LET, an observation shared by Lehujeur *et al.* (2021).

We observe the most prominent low-velocity anomaly for the two methods at 6–8 km depth. Jiwani-Brown *et al.* (2022) speculate this to be a singular magmatic body, surrounded by a complex, ductile mush. Based on the LET imaging, we instead speculate that this is a collection of cooling (low V_P) and hot (low V_S, high V_P/V_S) magmatic features, forming at similar depths, supplying the volcanic edifices of the ITVC separately. This singular anomaly recovered by Jiwani-Brown *et al.* (2022) could be a consequence of the horizontal smoothing applied in our two-step ANT inversion approach, and also the depreciation of resolution with depth. We could also attribute the depreciation of resolution to parametrizing the 3-D depth inversion into six initial layers, performed by Jiwani-Brown *et al.* (2022). Topography may also affect our results, with many major LET anomalies apparent in the 3 km asl. Areas of high relief can cause distortion in depth distributions of velocity structures, effectively shortening the effective path along which the surface wave will propagate, causing a decrease in the observed velocities within regions of topographic variations (Wang & Sun 2019). However, Wang *et al.* (2017) suggested that surface waves were not detrimentally sensitive to similar variations in topography we see in our study. They conclude that only low-period (<4 s) Rayleigh waves are affected, and even then, only by a negligible amount relative to the retrieved velocity anomalies. We see from Fig. 9 coherence between the two model outputs. It is only when we recover the V_P/V_S ratios that this discrepancy becomes most apparent. Given that surface waves should provide good resolution at shallow depths, this is countered by the suppression of velocities that would occur in the volcanic edifice, into the shallower few kilometres below 0 km depth. Despite this, we still observe the same proposed shallow, cooled magmatic body, observable from high V_P and V_S velocity anomalies, at 1 km depth of both ANT cross-sections (Figs 9g and h). There are differences in resolution between the two inversion methods. However, we do see similarities to suggest that the proposed concept within this study holds true. Similarities between ambient noise and local earthquake imaging methods are observed in volcanic environments at Avacha (Koulakov *et al.* 2014; Bushenkova *et al.* 2019), Katla (Jeddi *et al.* 2016, 2017), Toba (Stankiewicz *et al.* 2010; Koulakov *et al.* 2016), Klyuchevskoy (Koulakov *et al.* 2011; Green *et al.* 2020) and also in other tectonic environments (e.g. Shomali & Shirzad 2015; Lehujeur *et al.* 2021) where comparable velocity anomalies were found.

Fig. 10 presents our conceptual model of the ITVC, mainly derived from local earthquake tomographic inversions. We propose a trans-crustal structure consisting of the emplacement of magmatic bodies over various timescales, existing within a ductile domain. The nature of such a system is described by Christopher *et al.* (2015), Cashman *et al.* (2017) and Edmonds *et al.* (2019) as a large region of transient vertical melt transfer from the lower to the upper crust. We suggest that this diverse combination of cooled and hot magmatic bodies helps facilitate deformation associated with regional-scale oblique subduction and the formation of the forearc sliver and Panama microplate tectonic blocks. Jiwani-Brown (2023) support this observation from locally inverted focal mechanisms and principal horizontal stress calculations. There is evidence for a second stage of magma transfer from the lower to mid/upper crust beneath the proposed emplaced magmatic bodies, evident from the continuation of Anomaly 1 and Anomaly 2 to depths of 12 km and greater. This region of magma transfer is at the limits of our vertical resolution; however, it does coincide with a low-velocity region of the ANT (Jiwani-Brown *et al.* 2022) at similar depths beneath the intermediate depth reservoir. Interpreted by a markedly lower V_P to V_S velocity, we speculate that the anomaly at 6 km below Irazú is undergoing a liquid-to-gas phase transition, instigated by cooling and decompression of magmatic fluids (Table 1). Hydrothermal alteration could also be responsible for increasing the proportion of gas-phase fluids and decreasing permeability (Epiard *et al.* 2017). Although Irazú is not currently active, Mick *et al.* (2021) observed that magmatic–hydrothermal interactions with alteration minerals led to hydrothermal sealing and subsequent phreatic eruptions beneath Turrialba. If upwelling magmatic fluid were to re-accumulate beneath the Irazú volcano, we could observe similar eruptive activity to that of the neighbouring Turrialba volcano. An additional intruded magmatic body occurs below the edifice of Turrialba at 6–8 km depths, where anomalies of low V_S and high V_P/V_S ratio indicate the potential for partial melt. We speculate that this younger magmatic body is the system responsible for continued activity at Turrialba, in the form of degassing from upward migrating volcanic fluid (Conde *et al.* 2014; de Moor *et al.* 2016; van der Laat *et al.* 2022).

6 CONCLUSIONS

We constructed three 3-D seismic models of the ITVC using LET. We compared our results to previous ANT obtained with data recorded on the same seismic network, over the same period between April 2018 and March 2019. The ANT model contains V_S velocities, and the LET models contain V_P and V_S velocities and the ratio of these two parameters.

We observe two prominent contrasting anomalies beneath the Irazú and Turrialba volcanoes at depths of 8 km. The anomaly below Irazú has low V_P and low V_P/V_S ratios (as low as 1.60) that we associate with a cooling, previously intruded magmatic fluid undergoing hydrothermal alteration and a phase change from liquid to gas. The upper limit of the anomaly below Irazú at 6 km depth coincides with a cluster of seismicity we attribute to degassing from decompression. The anomaly below Turrialba has low V_S and high V_P/V_S ratios (reaching 1.85) that we associate with recently emplaced, active magmatic liquids responsible for the current surface activity of Turrialba. We interpret the subvertical cluster of seismicity at the upper limit of this anomaly to the upward migration of fluid between the magma reservoir and the surface caldera. Corresponding low V_P and V_S anomalies suggest a shared reservoir with a complex anatomy of multiphase fluids and temporarily varying magma emplacement.

Two high V_P/V_S ratio anomalies at 1–2 km below the summit of each volcano are attributed to the interaction of upward migrating fluids and hydrothermal systems directly below both Irazú and Turrialba. Similar values of high V_P/V_S ratio anomalies on the flanks of the volcanoes are attributed to the deep percolation of meteoric water in regions of high precipitation and denser river systems.

We present high V_P and V_S and low V_P/V_S ratio anomalies at 2 km asl between the two volcanic centres. These are interpreted as ancient, dried magmatic intrusions associated with the Finca Libres volcanic depression, formed during eruptive periods in the Quaternary.

Our comparison between LET and ANT methods reveals remarkable compliance of spatially located velocity anomalies at both intermediate and shallow depths. This compliance provides confidence in the two methods for imaging complex, heterogeneous structures such as volcanic systems. We present improvements in the lateral resolution achieved by the LET, and also a more detailed interpretation of the fluid content and active state of magmatism beneath the ITVC. The ANT provides improved depth resolution, allowing us to interpret the lower limit of the magmatic systems at 10 km depth.

ACKNOWLEDGMENTS

This work was supported by a grant from the Swiss National Science Foundation (GENERATE, grant number 166900, PI Matteo Lupi). Seismic instrumentation of the RSN and the OVSICORI is financed by the National Emergency Law No. 8488. The maintenance of the RSN seismic stations comes from the project funded by the Vicerrectoría de Investigación of the Universidad de Costa Rica: 'Geofísica y Geodinámica Interna del Arco Volcánico de Costa Rica (113-B5-A00)' and 'Programa de Investigación Red Sismológica Nacional (113-B9-911)'. Field work from OVSICORI was supported by project 0208-16 'Vigilancia de los volcanes de Costa Rica por medio de la actividad sísmica'. JFP and MM would like to thank the technical support provided by Christian Garita, Antonio Mata, Daniel Rojas and Hairo Villalobos (OVSICORI) and Luis Fernando Brenes and Jean Paul Calvo (RSN).

DATA AVAILABILITY

All data and models presented in the paper can be reproduced with the use of the full version of the LOTOS code provided by Ivan Koulakov at DOI: 10.5281/zenodo.7777962. Data from all stations (temporary and permanent) for the acquisition period of April 2018 to March 2019 can be found at DOI: 10.5281/zenodo.4912497.

SUPPORTING INFORMATION

Supplementary data are available at *GJI* online.

suppl_data

Please note: Oxford University Press is not responsible for the content or functionality of any supporting materials supplied by the authors. Any queries (other than missing material) should be directed to the corresponding author for the paper.

REFERENCES

Abers, G.A., Fischer, K., Hirth, G., Wiens, D., Plank, T., Holtzman, B.K., McCarthy, C. & Gazel, E., 2014. Reconciling mantle attenuation–temperature relationships from seismology, petrology, and laboratory measurements, *Geochem. Geophys. Geosyst.,* **15**(9), 3521–3542.

Adam, L. & Otheim, T., 2013. Elastic laboratory measurements and modeling of saturated basalts, *J. geophys. Res.,* **118**(3), 840–851.

Alvarado, G.E., Carr, M., Turrin, B.D., Swisher, C.C., Schmincke, H. & Hudnut, K.W., 2006. Recent volcanic history of Irazú volcano, Costa Rica: alternation and mixing of two magma batches, and pervasive mixing, *Spec. Pap. Geol. Soc. Am.,* **412,** 259. DOI: 10.1130/2006.2412(14).

Alvarado, G.E., Soto, G., Pullinger, C.R., Escobar, R., Bonis, S., Escobar, D. & Navarro, M., 2007. Volcanic activity, hazards, and monitoring, in Bundschuh, Jochen & E., Guillermo(eds.), *Central America: Geology, Resources and Hazards,* Vol. 2, pp. Routledge Taylor & Francis Group 1155–1188.

Alvarado, G.E. *et al.*, 2017. The new Central American seismic hazard zonation: mutual consensus based on up to day seismotectonic framework, *Tectonophysics,* **721,** 462–476. DOI: 10.1016/j.tecto.2017.10.013.

Álvarez-Gómez, J.A., Vázquez, A.S., Martínez-Díaz, J.J., Canora, C., Alonso-Henar, J., Insua-Arévalo, J.M. & Béjar-Pizarro, M., 2019. Push-pull driving of the Central America Forearc in the context of the Cocos–Caribbean–North America triple junction, *Sci. Rep.,* **9**(1), 1–13.

Arroyo, I.G., Husen, S., Flueh, E.R., Gossler, J., Kissling, E. & Alvarado, G.E., 2009. Three-dimensional *P*-wave velocity structure on the shallow part of the Central Costa Rican Pacific margin from local earthquake tomography using off- and onshore networks, *Geophys. J. Int.,* **179**(2), 827–849.

Battaglia, M. *et al.*, 2019. Monitoring volcanic deformation, in Şen, Zekâi & Almazroui, Mansour(eds.), *Reference Module in Earth Systems and Environmental Sciences,* Elsevier B. 774–804

Benjamin, E.R., Plank, T., Wade, J.A., Kelley, K.A., Hauri, E.H. & Alvarado, G.E., 2007. High water contents in basaltic magmas from Irazú volcano, Costa Rica, *J. Volc. Geotherm. Res.,* **168**(1–4), 68–92.

Berger, P., Got, J.-L., González, C.V. & Monteiller, V., 2011. Seismic tomography at popocatépetl volcano, mexico, *J. Volc. Geotherm. Res.,* **200**(3–4), 234–244.

Brenguier, F., Shapiro, N.M., Campillo, M., Nercessian, A. & Ferrazzini, V., 2007. 3-D surface wave tomography of the Piton de la Fournaise volcano using seismic noise correlations, *Geophys. Res. Lett.,* **34**(2).

Brenguier, F., Rivet, D., Obermann, A., Nakata, N., Boué, P., Lecocq, T., Campillo, M. & Shapiro, N., 2016. 4-D noise-based seismology at volcanoes: ongoing efforts and perspectives, *J. Volc. Geotherm. Res.,* **321,** 182–195. DOI: 10.1016/j.jvolgeores.2016.04.036.

Bushenkova, N., Koulakov, I., Senyukov, S., Gordeev, E.I., Huang, H.-H., El Khrepy, S. & Al Arifi, N., 2019. Tomographic images of magma chambers beneath the Avacha and Koryaksky volcanoes in Kamchatka, *J. geophys. Res.,* **124**(9), 9694–9713.

Calò, M., Di Luccio, F., Persaud, P. & Ventura, G., 2023. Ambient noise tomography of the Lipari volcanic island (Southern Italy) from a dense nodal array, *Geophys. Res. Lett.,* **50**(4), e2022GL101022.

Camacho, E., Hutton, W. & Pacheco, J., 2010. A new look at evidence for a Wadati–Benioff zone and active convergence at the north Panama deformed belt, *Bull. seism. Soc. Am.,* **100**(1), 343–348.

Campion, R. *et al.*, 2012. Space-and ground-based measurements of sulphur dioxide emissions from Turrialba volcano (Costa Rica), *Bull. Volcanol.,* **74**(7), 1757–1770.

Carr, M., Feigenson, M., Patino, L. & Walker, J., 2003. Volcanism and geochemistry in Central America: progress and problems, *Geophys. Monogr. Am. Geophys. Un.,* **138,** 153–174. DOI: 10.1029/138GM09.

Carr, M., Patino, L.C. & Feigenson, M.D., 2007. Petrology and geochemistry of lavas, Bundschuh, Jochen & Alvarado, Guillermo E.(eds.), In: *Central America: Geology, Resources and Hazards, published by Routledge Taylor & Francis Group,* Vol 1, pp. 565–577.

Carvajal-Soto, L.A., Ito, T., Protti, M. & Kimura, H., 2020. Earthquake potential in Costa Rica using three scenarios for the central Costa Rica deformed belt as western boundary of the Panama microplate, *J. South Am. Earth Sci.,* **97,** 102375. DOI: 10.1016/j.jsames.2019.102375.

Cashman, K.V., Sparks, R. S.J. & Blundy, J.D., 2017. Vertically extensive and unstable magmatic systems: a unified view of igneous processes, *Science,* **355**(6331).

Chen, H., Li, Z., Luo, Z., Ojo, A.O., Xie, J., Bao, F., Wang, L. & Tu, G., 2021. Crust and upper mantle structure of the South China Sea and adjacent areas from the joint inversion of ambient noise and earthquake surface wave dispersions, *Geochem. Geophys. Geosyst.,* **22**(3), e2020GC009356.

Christensen, N.I., 1996. Poisson's ratio and crustal seismology, *J. geophys. Res.,* **101**(B2), 3139–3156.

Christopher, T., Blundy, J., Cashman, K., Cole, P., Edmonds, M., Smith, P., Sparks, R. & Stinton, A., 2015. Crustal-scale degassing due to magma system destabilization and magma-gas decoupling at Soufrière Hills Volcano, Montserrat, *Geochem. Geophys. Geosyst.,* **16**(9), 2797–2811.

Conde, V., Bredemeyer, S., Duarte, E., Pacheco, J.F., Miranda, S., Galle, B. & Hansteen, T.H., 2014. SO_2 degassing from Turrialba Volcano linked to seismic signatures during the period 2008–2012, *Int. J. Earth Sci.,* **103**(7), 1983–1998.

Correa-Mora, F. *et al.*, 2009. GPS-derived coupling estimates for the Central America subduction zone and volcanic arc faults: El Salvador, Honduras and Nicaragua, *Geophys. J. Int.,* **179**(3), 1279–1291.

Coulon, C.A., Hsieh, P.A., White, R., Lowenstern, J.B. & Ingebritsen, S.E., 2017. Causes of distal volcano-tectonic seismicity inferred from hydrothermal modeling, *J. Volc. Geotherm. Res.,* **345,** 98–108. DOI: 10.1016/j.jvolgeores.2017.07.011.

Crawford, W.C., Rai, A., Singh, S.C., Cannat, M., Escartin, J., Wang, H., Daniel, R. & Combier, V., 2013. Hydrothermal seismicity beneath the summit of Lucky Strike volcano, Mid-Atlantic Ridge, *Earth planet. Sci. Lett.,* **373,** 118–128. DOI: 10.1016/j.epsl.2013.04.028.

de Moor, J.M. *et al.*, 2016. Turmoil at Turrialba volcano (Costa Rica): degassing and eruptive processes inferred from high-frequency gas monitoring, *J. geophys. Res.,* **121**(8), 5761–5775.

De Siena, L., Del Pezzo, E. & Bianco, F., 2010. Seismic attenuation imaging of Campi Flegrei: evidence of gas reservoirs, hydrothermal basins, and feeding systems, *J. geophys. Res.,* **115**(B9).

DeMets, C., 2001. A new estimate for present-day Cocos-–Caribbean plate motion: implications for slip along the Central American volcanic arc, *Geophys. Res. Lett.,* **28**(21), 4043–4046.

DeMets, C., Gordon, R.G. & Argus, D.F., 2010. Geologically current plate motions, *Geophys. J. Int.,* **181**(1), 1–80.

Denyer, P., 2009. *Atlas Tectónico de Costa Rica, Serie Reportes técnicos,* Editorial de la Universidad de Costa Rica.

DeShon, H.R. *et al.*, 2006. Seismogenic zone structure beneath the Nicoya Peninsula, Costa Rica, from three-dimensional local earthquake *P*- and *S*-wave tomography, *Geophys. J. Int.,* **164**(1), 109–124.

DeVitre, C.L., Gazel, E., Allison, C.M., Soto, G., Madrigal, P., Alvarado, G.E. & Lücke, O.H., 2019. Multi-stage chaotic magma mixing at Turrialba volcano, *J. Volc. Geotherm. Res.,* **381,** 330–346. DOI: 10.1016/j.jvolgeores.2019.06.011.

Di Piazza, A., Rizzo, A., Barberi, F., Carapezza, M., De Astis, G., Romano, C. & Sortino, F., 2015. Geochemistry of the mantle source and magma feeding system beneath Turrialba volcano, Costa Rica, *Lithos,* **232,** 319–335. DOI: 10.1016/j.lithos.2015.07.012.

Di Piazza, A., Vona, A., Mollo, S., De Astis, G., Soto, G.J. & Romano, C., 2019. Unsteady magma discharge during the "El Retiro" subplinian eruption (Turrialba volcano, Costa Rica): insights from textural and petrological analyses, *J. Volc. Geotherm. Res.,* **371,** 101–115.

Dinc, A.N., Koulakov, I., Thorwart, M., Rabbel, W., Flueh, E.R., Arroyo, I., Taylor, W. & Alvarado, G., 2010. Local earthquake tomography of central Costa Rica: transition from seamount to ridge subduction, *Geophys. J. Int.,* **183**(1), 286–302.

Dzierma, Y., Thorwart, M.M., Rabbel, W., Flueh, E.R., Alvarado, G. & Mora, M., 2010. Imaging crustal structure in south central Costa Rica with receiver functions, *Geochem. Geophys. Geosyst.,* **11**(8).

Dzierma, Y., Rabbel, W., Thorwart, M.M., Flueh, E.R., Mora, M. & Alvarado, G.E., 2011. The steeply subducting edge of the Cocos Ridge: evidence from receiver functions beneath the northern Talamanca range, south-central Costa Rica, *Geochem. Geophys. Geosyst.,* **12**(4).

Ebmeier, S. *et al.*, 2018. Synthesis of global satellite observations of magmatic and volcanic deformation: implications for volcano monitoring & the lateral extent of magmatic domains, *J. Appl. Volcanol.,* **7**(1), 1–26.

Edmonds, M., Cashman, K.V., Holness, M. & Jackson, M., 2019. Architecture and dynamics of magma reservoirs Philosophical Transactions of the Royal Society A 377(2139) p.20180298.

Egorushkin, I., Koulakov, I.Y., Shapiro, N., Gordeev, E., Yakovlev, A. & Abkadyrov, I., 2021. Structure of the upper crust beneath the Klyuchevskoy group of volcanoes revealed from ambient noise tomography, *Russ. Geol. Geophys.,* **62**(1), 68–82.

Epiard, M., Avard, G., de Moor, J.M., Martinez Cruz, M., Barrantes Castillo, G. & Bakkar, H., 2017. Relationship between diffuse CO2 degassing and volcanic activity. Case study of the Poás, Irazú, and Turrialba Volcanoes, Costa Rica, *Front. Earth Sci.,* **5,** 71. DOI: 10.3389/feart.2017.00071.

Fallahi, M.J., Obermann, A., Lupi, M., Karyono, K. & Mazzini, A., 2017. The plumbing system feeding the Lusi eruption revealed by ambient noise tomography, *J. geophys. Res.,* **122**(10), 8200–8213.

Franco, A. *et al.*, 2012. Fault kinematics in northern Central America and coupling along the subduction interface of the Cocos Plate, from GPS data in Chiapas (Mexico), Guatemala and El Salvador, *Geophys. J. Int.,* **189**(3), 1223–1236.

Freymueller, J.T., Kellogg, J.N. & Vega, V., 1993. Plate motions in the North Andean region, *J. geophys. Res.,* **98**(B12), 21 853–21 863.

Gao, L., Zhang, H., Gao, L., He, C., Xin, H. & Shen, W., 2022. High-resolution Vs tomography of South China by joint inversion of body wave and surface wave data, *Tectonophysics,* **824,** 229228. DOI: 10.1016/j.tecto.2022.229228.

García, M., Vargas, C. & Koulakov, I.Y., 2019. Local earthquake tomography of the Nevado del Huila Volcanic Complex (Colombia): magmatic and tectonic interactions in a volcanic-glacier complex system, *J. geophys. Res.,* **124**(2), 1688–1699.

Gazel, E., Carr, M., Hoernle, K., Feigenson, M.D., Szymanski, D., Hauff, F. & Van Den Bogaard, P., 2009. Galapagos-OIB signature in southern Central America: mantle refertilization by arc–hot spot interaction, *Geochem. Geophys. Geosyst.,* **10**(2).

Gazel, E., Hayes, J.L., Ulloa, A., Alfaro, A., Coleman, D.S. & Carr, M., 2019. The record of the transition from an oceanic arc to a young continent in the Talamanca Cordillera, *Geochem. Geophys. Geosyst.,* **20**(6), 2733–2752.

Gazel, E., Flores, K.E. & Carr, M., 2021. Architectural and Tectonic Control on the Segmentation of the Central American Volcanic Arc, *Annu. Rev. Earth Planet. Sci.,* **49,** 495–521. DOI: 10.1146/annurev-earth-082420-055108.

Geoffroy, L. & Dorbath, C., 2008. Deep downward fluid percolation driven by localized crust dilatation in Iceland, *Geophys. Res. Lett.,* **35**(17).

González-Vidal, D., Obermann, A., Tassara, A., Bataille, K. & Lupi, M., 2018. Crustal model of the Southern Central Andes derived from ambient seismic noise Rayleigh-wave tomography, *Tectonophysics,* **744,** 215–226. DOI: 10.1016/j.tecto.2018.07.004.

Green, R.G. *et al.*, 2020. Magmatic and sedimentary structure beneath the Klyuchevskoy volcanic group, Kamchatka, from ambient noise tomography, *J. geophys. Res.,* **125**(3), e2019JB018900.

Harmon, N., Gerstoft, P., Rychert, C.A., Abers, G.A., Salas de La Cruz, M. & Fischer, K.M., 2008. Phase velocities from seismic noise using beamforming and cross correlation in Costa Rica and Nicaragua, *Geophys. Res. Lett.,* **35**(19).

Hartzell, S., Meremonte, M., Ramírez-Guzmán, L. & McNamara, D., 2014. Ground motion in the presence of complex topography: Earthquake and ambient noise sources, *Bull. seism. Soc. Am.,* **104**(1), 451–466.

Haslinger, F., Thurber, C., Mandernach, M. & Okubo, P., 2001. Tomographic image of P-velocity structure beneath Kilauea's East Rift Zone and South Flank: Seismic evidence for a deep magma body, *Geophys. Res. Lett.,* **28**(2), 375–378.

Heap, M., Lavallée, Y., Petrakova, L., Baud, P., Reuschle, T., Varley, N. & Dingwell, D.B., 2014. Microstructural controls on the physical and mechanical properties of edifice-forming andesites at volcán de colima, mexico, *J. geophys. Res.,* **119**(4), 2925–2963.

Heap, M.J. & Violay, M.E., 2021. The mechanical behaviour and failure modes of volcanic rocks: a review, *Bull. Volcanol.,* **83**(5), 1–47.

Heap, M.J., Coats, R., Chen, C.-f., Varley, N., Lavallée, Y., Kendrick, J., Xu, T. & Reuschlé, T., 2018. Thermal resilience of microcracked andesitic dome rocks, *J. Volc. Geotherm. Res.,* **367,** 20–30. DOI: 10.1016/j.jvolgeores.2018.10.021.

Hoernle, K. *et al.*, 2008. Arc-parallel flow in the mantle wedge beneath Costa Rica and Nicaragua, *Nature,* **451**(7182), 1094–1097.

Husen, S., Quintero, R., Kissling, E. & Hacker, B., 2003. Subduction-zone structure and magmatic processes beneath Costa Rica constrained by local earthquake tomography and petrological modelling, *Geophys. J. Int.,* **155**(1), 11–32.

Iyer, H. & Hirahara, K., 1993. *Seismic Tomography: Theory and Practice,* Springer Science & Business Media.

Jaxybulatov, K., Shapiro, N., Koulakov, I., Mordret, A., Landès, M. & Sens-Schönfelder, C., 2014. A large magmatic sill complex beneath the Toba caldera, *Science,* **346**(6209), 617–619.

Jeddi, Z., Tryggvason, A. & Gudmundsson, Ó., 2016. The Katla volcanic system imaged using local earthquakes recorded with a temporary seismic network, *J. geophys. Res.,* **121**(10), 7230–7251.

Jeddi, Z., Gudmundsson, O. & Tryggvason, A., 2017. Ambient-noise tomography of Katla volcano, South Iceland, *J. Volc. Geotherm. Res.,* **347,** 264–277. DOI: 10.1016/j.jvolgeores.2017.09.019.

Jiwani-Brown, E., 2023. The Anatomy of a Magmatic System, Revealed by Multi-Disciplinary Seismological Methods in Central Costa Rica, *PhD thesis,* Faculté des sciences, Section des sciences de la Terre et de l'Environnement, Département des sciences de la Terre, Université de Genève.

Jiwani-Brown, E., Planès, T., Pacheco, J.F., Mora, M.M. & Lupi, M., **Vol. 127,** 2022. Magmatic and tectonic domains of central costa rica and the Irazú–Turrialba volcanic complex revealed by ambient noise tomography, *J. geophys. Res.,* e2022JB024575.

Kasatkina, E., Koulakov, I., West, M. & Izbekov, P., 2014. Seismic structure changes beneath Redoubt Volcano during the 2009 eruption inferred from local earthquake tomography, *J. geophys. Res.,* **119**(6), 4938–4954.

Kellogg, J.N., Vega, V., Stallings, T. & Aiken, C.L., 1995. Tectonic development of Panama, Costa Rica, and the Colombian Andes: constraints from global positioning system geodetic studies and gravity, *Spec. Pap. Geol. Soc. Am.,* 75–75.

Kissling, E., Ellsworth, W., Eberhart-Phillips, D. & Kradolfer, U., 1994. Initial reference models in local earthquake tomography, *J. geophys. Res.,* **99**(B10), 19 635–19 646.

Kissling, E., Kradolfer, U. & Maurer, H., 1995. *Program VELEST User's Guide-Short Introduction,* Institute of Geophysics, ETH Zurich.

Kobayashi, D., LaFemina, P., Geirsson, H., Chichaco, E., Abrego, A.A., Mora, H. & Camacho, E., 2014. Kinematics of the western Caribbean: Collision of the Cocos Ridge and upper plate deformation, *Geochem. Geophys. Geosyst.,* **15**(5), 1671–1683.

Koulakov, I., 2009. LOTOS code for local earthquake tomographic inversion: Benchmarks for testing tomographic algorithms, *Bull. seism. Soc. Am.,* **99**(1), 194–214.

Koulakov, I. *et al.*, 2007. P and S velocity structure of the crust and the upper mantle beneath central Java from local tomography inversion, *J. geophys. Res.,* **112**(B8).

Koulakov, I., Bindi, D., Parolai, S., Grosser, H. & Milkereit, C., 2010. Distribution of seismic velocities and attenuation in the crust beneath the North Anatolian Fault (Turkey) from local earthquake tomography, *Bull. seism. Soc. Am.,* **100**(1), 207–224.

Koulakov, I., Gordeev, E.I., Dobretsov, N.L., Vernikovsky, V.A., Senyukov, S. & Jakovlev, A., 2011. Feeding volcanoes of the Kluchevskoy group from the results of local earthquake tomography, *Geophys. Res. Lett.,* **38**(9).

Koulakov, I., Gordeev, E.I., Dobretsov, N.L., Vernikovsky, V.A., Senyukov, S., Jakovlev, A. & Jaxybulatov, K., 2013. Rapid changes in magma storage beneath the Klyuchevskoy group of volcanoes inferred from time-dependent seismic tomography, *J. Volc. Geotherm. Res.,* **263,** 75–91. DOI: 10.1016/j.jvolgeores.2012.10.014.

Koulakov, I. *et al.*, 2014. Asymmetric caldera-related structures in the area of the Avacha group of volcanoes in Kamchatka as revealed by ambient noise tomography and deep seismic sounding, *J. Volc. Geotherm. Res.,* **285,** 36–46. DOI: 10.1016/j.jvolgeores.2014.08.012.

Koulakov, I., Kasatkina, E., Shapiro, N.M., Jaupart, C., Vasilevsky, A., El Khrepy, S., Al-Arifi, N. & Smirnov, S., 2016. The feeder system of the Toba supervolcano from the slab to the shallow reservoir, *Nat. Commun.,* **7**(1), 1–12.

Koulakov, I. *et al.*, 2017. Three different types of plumbing system beneath the neighboring active volcanoes of Tolbachik, Bezymianny, and Klyuchevskoy in Kamchatka, *J. geophys. Res.,* **122**(5), 3852–3874.

Koulakov, I., Smirnov, S., Gladkov, V., Kasatkina, E., West, M., El Khrepy, S. & Al-Arifi, N., 2018. Causes of volcanic unrest at Mt. Spurr in 2004–2005 inferred from repeated tomography, *Sci. Rep.,* **8**(1), 1–7.

Koulakov, I., Boychenko, E. & Smirnov, S.Z., 2020a. Magma chambers and meteoric fluid flows beneath the Atka volcanic complex (Aleutian Islands) inferred from local earthquake tomography, *Geosciences,* **10**(6), 214.

Koulakov, I. *et al.*, 2020b. Mantle sources of magmatic activity in the Northern group of volcanoes in Kamchatka inferred from earthquake tomography, *J. geophys. Res.,* **10,** e2020JB020097. DOI: 10.1029/2020JB020097.

Koulakov, I. *et al.*, 2021. Anatomy of the Bezymianny volcano merely before an explosive eruption on 20.12. 2017, *Sci. Rep.,* **11**(1), 1–12.

Kuznetsov, P. & Koulakov, I.Y., 2014. The three-dimensional structure beneath the Popocatépetl volcano (Mexico) based on local earthquake seismic tomography, *J. Volc. Geotherm. Res.,* **276,** 10–21. DOI: 10.1029/2020JB020097.

Kuznetsov, P.Y. *et al.*, 2017. Structure of volatile conduits beneath Gorely Volcano (Kamchatka) revealed by local earthquake tomography, *Geosciences,* **7**(4), 111.

LaFemina, P. *et al.*, 2009. Fore-arc motion and Cocos Ridge collision in Central America, *Geochem. Geophys. Geosyst.,* **10**(5).

Lees, J.M., 2007. Seismic tomography of magmatic systems, *J. Volc. Geotherm. Res.,* **167**(1–4), 37–56.

Lees, J.M. & Wu, H., 2000. Poisson's ratio and porosity at Coso geothermal area, California, *J. Volc. Geotherm. Res.,* **95**(1–4), 157–173.

Lehujeur, M., Vergne, J., Maggi, A. & Schmittbuhl, J., 2016. Ambient noise tomography with non-uniform noise sources and low aperture networks: case study of deep geothermal reservoirs in northern Alsace, France, *Geophys. Suppl. Mon. Not. R. Astron. Soc.,* **208**(1), 193–210.

Lehujeur, M., Chevrot, S., Villaseñor, A., Masini, E., Saspiturry, N., Lescoutre, R. & Sylvander, M., 2021. Three-dimensional shear velocity structure of the Mauléon and Arzacq basins (Western Pyrenees) structure tridimensionnelle des vitesses de cisaillement dans les bassins de mauléon et arzacq (pyrénées occidentales), *Bull. Soc. Géol. Fr.,* **192**(1). DOI: 10.1051/bsgf/2021039.

Lesage, P., Heap, M.J. & Kushnir, A., 2018. A generic model for the shallow velocity structure of volcanoes, *J. Volc. Geotherm. Res.,* **356,** 114–126. DOI: 10.1016/j.jvolgeores.2018.03.003.

Li, Y. & Thurber, C.H., 1995. Modelling of near-surface seismic structure beneath Hawaii using reverberations, *Geophys. J. Int.,* **122**(2), 441–456.

Lin, F., Moschetti, M. & Ritzwoller, M., 2008. Surface wave tomography of the western United States from ambient seismic noise: Rayleigh and Love wave phase velocity maps, *Geophys. J. Int.,* **173**(1), 281–298.

Lücke, O.H., Götze, H.-J. & Alvarado, G.E., 2010. A constrained 3D density model of the upper crust from gravity data interpretation for central Costa Rica, *Int. J. Geophys.,* **2010**.

Lundgren, P. & Russo, R., 1996. Finite element modeling of crustal deformation in the North America-Caribbean Plate Boundary Zone, *J. geophys. Res.,* **101**(B5), 11 317–11 327.

MacMillan, I., Gans, P.B. & Alvarado, G.E., 2004. Middle Miocene to present plate tectonic history of the southern Central American Volcanic Arc, *Tectonophysics,* **392**(1–4), 325–348.

Marshall, J.S., Fisher, D.M. & Gardner, T.W., 2000. Central Costa Rica deformed belt: kinematics of diffuse faulting across the western Panama block, *Tectonics,* **19**(3), 468–492.

Martini, F., Tassi, F., Vaselli, O., Del Potro, R., Martinez, M., Van del Laat, R. & Fernandez, E., 2010. Geophysical, geochemical and geodetical signals of reawakening at Turrialba volcano (Costa Rica) after almost 150 years of quiescence, *J. Volc. Geotherm. Res.,* **198**(3–4), 416–432.

Mick, E., Stix, J., de Moor, J.M. & Avard, G., 2021. Hydrothermal alteration and sealing at Turrialba volcano, Costa Rica, as a mechanism for phreatic eruption triggering, *J. Volc. Geotherm. Res.,* **416,** 107297. DOI: 10.1016/j.jvolgeores.2021.107297.

Molnar, P. & Sykes, L.R., 1969. Tectonics of the Caribbean and Middle America regions from focal mechanisms and seismicity, *Bull. geol. Soc. Am.,* **80**(9), 1639–1684.

Montero, W., 2001. Neotectónica de la región central de Costa Rica: frontera oeste de la microplaca de Panamá, *Rev. Geol. Am. Central*.

Montero, W., Lewis, J.C., Marshall, J.S., Kruse, S. & Wetmore, P., 2013a. Neotectonic faulting and forearc sliver motion along the Atirro–Río Sucio fault system, Costa Rica, Central America, *Bull. geol. Soc. Am.,* **125**(5–6), 857–876.

Montero, W., Rojas, W. & Linkimer, L., 2013b. Neotectónica de las fallas Ochomogo y Capellades y su relación con el sistema de falla Aguacaliente, falda sur macizo Irazú-Turrialba, Costa Rica, *Rev. Geol. Am. Central,* **48,** 119–139.

Mordret, A., Landès, M., Shapiro, N., Singh, S., Roux, P. & Barkved, O., 2013. Near-surface study at the Valhall oil field from ambient noise surface wave tomography, *Geophys. J. Int.,* **193**(3), 1627–1643.

Nara, Y., Meredith, P.G., Yoneda, T. & Kaneko, K., 2011. Influence of macro-fractures and micro-fractures on permeability and elastic wave velocities in basalt at elevated pressure, *Tectonophysics,* **503**(1–2), 52–59.

Nicholson, C. & Simpson, D.W., 1985. Changes in Vp/Vs with depth: implications for appropriate velocity models, improved earthquake locations, and material properties of the upper crust, *Bull. seism. Soc. Am.,* **75**(4), 1105–1123.

Nicolson, H., Curtis, A., Baptie, B. & Galetti, E., 2012. Seismic interferometry and ambient noise tomography in the British Isles, *Proc. Geologists' Assoc.,* **123**(1), 74–86.

Norabuena, E. *et al.*, 2004. Geodetic and seismic constraints on some seismogenic zone processes in Costa Rica, *J. geophys. Res.,* **109**(B11).

Nuñez, E., Schimmel, M., Stich, D. & Iglesias, A., 2020. Crustal velocity anomalies in Costa Rica from ambient noise tomography, *Pure appl. Geophys.,* **177**(2), 941–960.

OVSICORI-UNA, 2020. Boletín anual del programa de vigilancia volcánica, año 2020. tech. rep. observatorio vulcanológico sismológico de costa rica, universidad nacional, heredia, costa rica, *OVSICORI-UNA Boletín 2020*.

Paige, C.C. & Saunders, M.A., 1982. LSQR: an algorithm for sparse linear equations and sparse least squares, *ACM Trans. Math. Softw.,* **8**(1), 43–71.

Parolai, S., Bindi, D. & Trojani, L., 2001. Site response for the RSM seismic network and source parameters in the Central Apennines (Italy), *Pure appl. Geophys.,* **158**(4), 695–715.

Planès, T., Obermann, A., Antunes, V. & Lupi, M., 2020. Ambient-noise tomography of the Greater Geneva Basin in a geothermal exploration context, *Geophys. J. Int.,* **220**(1), 370–383.

Pola, A., Crosta, G., Fusi, N., Barberini, V. & Norini, G., 2012. Influence of alteration on physical properties of volcanic rocks, *Tectonophysics,* **566,** 67–86.

Protti, M., Schwartz, S.Y. & Zandt, G., 1996. Simultaneous inversion for earthquake location and velocity structure beneath central Costa Rica, *Bull. seism. Soc. Am.,* **86**(1A), 19–31.

Quintero, R. & Kissling, E., 2001. An improved P-wave velocity reference model for Costa Rica, *Geofis. Int.,* **40**(1), 3–19.

Rabbel, W., Koulakov, I., Dinc, A.N. & Jakovlev, A., 2011. Arc-parallel shear deformation and escape flow in the mantle wedge of the Central America subduction zone: evidence from P wave anisotropy, *Geochem. Geophys. Geosyst.,* **12**(5).

Rawlinson, N. & Spakman, W., 2016. On the use of sensitivity tests in seismic tomography, *Geophys. J. Int.,* **205**(2), 1221–1243.

Rawlinson, N., Fichtner, A., Sambridge, M. & Young, M.K., 2014. Seismic tomography and the assessment of uncertainty, *Adv. Geophys.,* **55,** 1–76. DOI: 10.1016/bs.agph.2014.08.001.

Reagan, M., Duarte, E., Soto, G.J. & Fernández, E., 2006. The eruptive history of Turrialba volcano, Costa Rica, and potential hazards from future eruptions, *Spec. Pap. Geol. Soc. Am.,* **412,** 235.

Rizzo, A.L., Di Piazza, A., de Moor, J.M., Alvarado, G.E., Avard, G., Carapezza, M.L. & Mora, M.M., 2016. Eruptive activity at Turrialba volcano (Costa Rica): inferences from $^{3}He/^{4}He$ in fumarole gases and chemistry of the products ejected during 2014 and 2015, *Geochem. Geophys. Geosyst.,* **17**(11), 4478–4494.

RSN, 2011. Network information, *FDSN Network Information,* Universidad de Costa Rica, TC: Red Simológica Nacional (RSN).

Rychert, C.A., Fischer, K.M., Abers, G.A., Plank, T., Syracuse, E., Protti, J., Gonzalez, V. & Strauch, W., 2008. Strong along-arc variations in attenuation in the mantle wedge beneath Costa Rica and Nicaragua, *Geochem. Geophys. Geosyst.,* **9**(10).

Sallarès, V., Dañobeitia, J.J. & Flueh, E., 2000. Seismic tomography with local earthquakes in Costa Rica, *Tectonophysics,* **329**(1–4), 61–78.

Shapiro, N., Campillo, M., Stehly, L. & Ritzwoller, M.H., 2005. High-resolution surface-wave tomography from ambient seismic noise, *Science,* **307**(5715), 1615–1618.

Shirzad, T. & Shomali, Z.-H., 2015. Extracting seismic body and Rayleigh waves from the ambient seismic noise using the rms-stacking method, *Seismol. Res. Lett.,* **86**(1), 173–180.

Shomali, Z.H. & Shirzad, T., 2015. Crustal structure of Damavand volcano, Iran, from ambient noise and earthquake tomography, *J. Seismol.,* **19**(1), 191–200.

Silver, E.A., Reed, D.L., Tagudin, J.E. & Heil, D.J., 1990. Implications of the north and south Panama thrust belts for the origin of the Panama orocline, *Tectonics,* **9**(2), 261–281.

Staller, A., Martínez-Díaz, J.J., Benito, B., Alonso-Henar, J., Hernandez, D., Hernandez-Rey, R. & Diaz, M., 2016. Present-day crustal deformation along the El Salvador Fault Zone from ZFESNet GPS network, *Tectonophysics,* **670,** 66–81. DOI: 10.1016/j.tecto.2015.12.017.

Stankiewicz, J., Ryberg, T., Haberland, C., Fauzi & Natawidjaja, D., 2010. Lake Toba volcano magma chamber imaged by ambient seismic noise tomography, *Geophys. Res. Lett.,* **37**(17).

Stoiber, R. & Carr, M., 1973. Quaternary volcanic and tectonic segmentation of Central America, *Bull. Volcanol.,* **37**(3), 304–325.

Sun, J., Colombo, D., Li, Y. & Shragge, J., 2020. Geophysics introduces new section on multiphysics and joint inversion, *Leading Edge,* **39**(10), 753–754.

Syracuse, E.M., Abers, G.A., Fischer, K., MacKenzie, L., Rychert, C., Protti, M., González, V. & Strauch, W., 2008. Seismic tomography and earthquake locations in the Nicaraguan and Costa Rican upper mantle, *Geochem. Geophys. Geosyst.,* **9**(7).

Takei, Y., 2002. Effect of pore geometry on VP/VS: From equilibrium geometry to crack, *J. geophys. Res.,* **107**(B2), ECV–6.

Thurber, C., Ritsema, J., Romanowicz, B. & Dziewonski, A., 2009. Theory and observations: seismic tomography and inversion methods, in *Treatise on Geophysics: Seismology and structure of the Earth,* pp. Elsevier B.V. 323–360.

Um, J. & Thurber, C., 1987. A fast algorithm for two-point seismic ray tracing, *Bull. seism. Soc. Am.,* **77**(3), 972–986.

van der Laat, L., Mora, M.M., Pacheco, J.F., Lesage, P. & Meneses, E., 2022. Seismicity during the recent activity (2009–2020) of Turrialba volcano, Costa Rica, *J. Volc. Geotherm. Res.,* **431,** 107651. DOI: 10.1016/j.jvolgeores.2022.107651.

Vanorio, T., Prasad, M., Patella, D. & Nur, A., 2002. Ultrasonic velocity measurements in volcanic rocks: correlation with microtexture, *Geophys. J. Int.,* **149**(1), 22–36.

Vargas, C., Koulakov, I., Jaupart, C., Gladkov, V., Gomez, E., El Khrepy, S. & Al-Arifi, N., 2017. Breathing of the Nevado del Ruiz volcano reservoir, Colombia, inferred from repeated seismic tomography, *Sci. Rep.,* **7**(1), 1–6.

Vaselli, O., Tassi, F., Duarte, E., Fernandez, E., Poreda, R. & Huertas, A.D., 2010. Evolution of fluid geochemistry at the Turrialba volcano (Costa Rica) from 1998 to 2008, *Bull. Volcanol.,* **72**(4), 397–410.

Villegas Alvarez, R.J., Petrinovic, I.A. & Carniel, R., 2019. S-wave velocity zones at the Irazú Volcano (Costa Rica), *J. South Am. Earth Sci.*.**90,** 314–324. DOI: 10.1016/j.jsames.2018.12.021.

Vinciguerra, S., Trovato, C., Meredith, P.G. & Benson, P.M., 2005. Relating seismic velocities, thermal cracking and permeability in Mt. Etna and Iceland basalts, *Int. J. Rock Mech. Min. Sci.,* **42**(7–8), 900–910.

Wang, S. & Sun, X., 2019. Topography effect on ambient noise tomography using a dense seismic array, *Earthq. Sci.,* **31**(5–6), 291–300.

Wang, Y., Lin, F.-C., Schmandt, B. & Farrell, J., 2017. Ambient noise tomography across Mount St. Helens using a dense seismic array, *J. geophys. Res.,* **122**(6), 4492–4508.

Waylen, P.R., Quesada, M.E. & Caviedes, C.N., 1996. Temporal and spatial variability of annual precipitation in Costa Rica and the Southern Oscillation, *Int. J. Climatol.,* **16**(2), 173–193.

Wilks, M., Kendall, J.-M., Nowacki, A., Biggs, J., Wookey, J., Birhanu, Y., Ayele, A. & Bedada, T., 2017. Seismicity associated with magmatism, faulting and hydrothermal circulation at Aluto Volcano, Main Ethiopian Rift, *J. Volc. Geotherm. Res.,* **340,** 52–67.

Wu, Z., Huang, J., Dustin, L. & Sadda, S., 2009. Signal strength is an important determinant of accuracy of nerve fiber layer thickness measurement by optical coherence tomography, *J. Glaucoma,* **18**(3), 213–216.

Xia, J., Miller, R.D. & Park, C.B., 2000. Advantages of calculating shear-wave velocity from surface waves with higher modes, in *SEG Technical Program Expanded Abstracts 2000,* pp. 1295–1298, Society of Exploration Geophysicists.

Yao, Z., Quintero, R. & Roberts, R., 1999. Tomographic imaging of *P*- and *S*-wave velocity structure beneath Costa Rica, *J. Seismol.,* **3**(2), 177–190.

Zhang, H., Maceira, M., Roux, P. & Thurber, C., 2014. Joint inversion of body-wave arrival times and surface-wave dispersion for three-dimensional seismic structure around SAFOD, *Pure appl. Geophys.,* **171**(11), 3013–3022.

Zhang, X., Roy, C., Curtis, A., Nowacki, A. & Baptie, B., 2020. Imaging the subsurface using induced seismicity and ambient noise: 3-D tomographic Monte Carlo joint inversion of earthquake body wave traveltimes and surface wave dispersion, *Geophys. J. Int.,* **222**(3), 1639–1655.